Impacts of Including Rain-Evaporative Cooling in the Initial Conditions on the Prediction of a Coastal Heavy Rainfall Event during TiMREX

CHUAN-CHI TU[a] AND YI-LENG CHEN

Department of Atmospheric Sciences, School of Ocean and Earth Science and Technology, University of Hawai'i at Mānoa, Honolulu, Hawaii

SHU-YA CHEN

University Corporation for Atmospheric Research, Boulder, Colorado, and GPS Science and Application Research Center, National Central University, Jhongli, Taiwan

YING-HWA KUO

University Corporation for Atmospheric Research, and National Center for Atmospheric Research, Boulder, Colorado

PAY-LIAM LIN

Department of Atmospheric Sciences, National Central University, Jhongli, Taiwan

(Manuscript received 14 June 2016, in final form 15 September 2016)

ABSTRACT

A cycling run, which began 36 h before the model forecast, was employed to assimilate special Terrain-influenced Monsoon Rainfall Experiment (TiMREX) soundings, Global Telecommunications System (GTS) data, and Constellation Observing System for Meteorology, Ionosphere and Climate (COSMIC) global positioning system (GPS) radio occultation (RO) refractivity profiles to improve the model initial conditions provided by the National Centers for Environmental Prediction (NCEP) Global Forecast System (GFS) to study a coastal, heavy rainfall event over southwestern Taiwan during 15–16 June 2008. The 36-h cycling run with data assimilation (DA_ALL_DATA run) has a positive impact on the depiction of subsynoptic flow in the model initial conditions at 1200 UTC 15 June, including the warm moist tongue and southwesterly monsoon flow over the open ocean. Furthermore, the cold pool caused by the evaporative cooling of antecedent rains and orographic blocking over southwestern Taiwan are better resolved in the nested high-resolution domain in the DA_ALL_DATA run as compared to the initial conditions provided by the NCEP GFS. As a result, the heavy rainfall along the southwestern coast and afternoon localized heavy rainfall over northern Taiwan are better predicted in the DA_ALL_DATA run.

Model sensitivity tests are also performed to diagnose the effects of terrain and rain-evaporative cooling on the intensity and depth of the cold pool and degree of orographic blocking on the southwesterly flow over southwestern Taiwan. It is apparent that including rain-evaporative cooling from antecedent rains and orographic effects in the model initial conditions are important to account for the predicted rainfall distribution of this coastal rainfall event.

Denotes Open Access content.

School of Ocean and Earth Science and Technology Contribution Number 9744.

[a] Current affiliation: Department of Atmospheric Sciences, National Central University, Jhongli, Taiwan.

Corresponding author address: Dr. Yi-Leng Chen, Department of Atmospheric Sciences, SOEST, University of Hawai'i at Mānoa, Honolulu, HI 96822.
E-mail: yileng@hawaii.edu

DOI: 10.1175/MWR-D-16-0224.1

1. Introduction

Under the prevailing southwesterly monsoon flow during the early summer rainy season over Taiwan both the hourly rainfall frequencies (Yeh and Chen 1998; Kerns et al. 2010) and climatological heavy rainfall occurrences (hourly rainfall rate > 15 mm h^{-1}) (e.g., Chien and Jou 2004; Chen et al. 2007; Ruppert et al. 2013) have a pronounced afternoon maximum on the southwestern windward slopes due to orographic lifting by the combined anabatic winds in low levels and the southwesterly flow aloft. Along the southwestern windward coast, rainfall occurrences are slightly more frequent in the early morning during the diurnal cycle (Yeh and Chen 1998; Kerns et al. 2010), possibly due to the convergence between the offshore flow and incoming decelerating southwesterly flow. The early morning rainfall maximum along the southwestern coast of Taiwan is not a regular daily occurrence (Kerns et al. 2010) due to flat terrain and relatively shallow (<200 m) land-breeze flow with a small thermal deficit ($\Delta\theta_v \sim$ 1–3 K), as compared to the upstream southwesterly flow (Tu et al. 2014).

In addition to the diurnal heating cycle, the rainfall and airflow over Taiwan during May and June is also affected by orographic blocking. Under the prefrontal southwesterly flow, island blocking and flow splitting occur off the southwestern coast of Taiwan with a windward ridge–leeside trough pressure pattern (Chen et al. 1989; Trier et al. 1990; Chen and Hui 1990; Chen and Li 1995a) in agreement with the theoretical studies of airflow past an isolated mountain for a low Froude number [$\mathrm{Fr} = U/Nh < O(1)$, where U is the basic wind speed, N is the Brunt–Väisälä frequency, and h is the mountain height] flow regime (Smolarkiewicz et al. 1988; Smith 1989; Sun et al. 1991). The orographic blocking and upstream flow deceleration are most significant in the early morning when the land surface temperature is the coldest (Chen and Li 1995b; Lin et al. 2011).

The main purpose of the joint U.S.–Taiwan Terrain-influenced Monsoon Rainfall Experiment (TiMREX) (15 May–30 June 2008) was to study multiple-scale physical processes leading to the development of localized heavy rainfall during the early summer rainy season, especially over the south-southwestern part of Taiwan. During the TiMREX intensive observing period (IOP) 8 (14–16 June), with rain-evaporative cooling due to antecedent rains, the cold pool in the early morning of 16 June reaches as deep as ~500 m with a thermal deficit of ~−5 K (Xu et al. 2012; Tu et al. 2014). Throughout the night, nocturnal showers occurred along the southwestern coast. The convective showers were enhanced offshore due to the warm, moist southwesterly flow being lifted by the cold pool with significant blocking off the southwestern coast (Xu et al. 2012; Tu et al. 2014; Wang et al. 2014a,b). Above the cold pool, the southwesterly flow is deflected by orographic blocking with a large wind component parallel to the terrain (Tu et al. 2014). Furthermore, with the continued drifting of

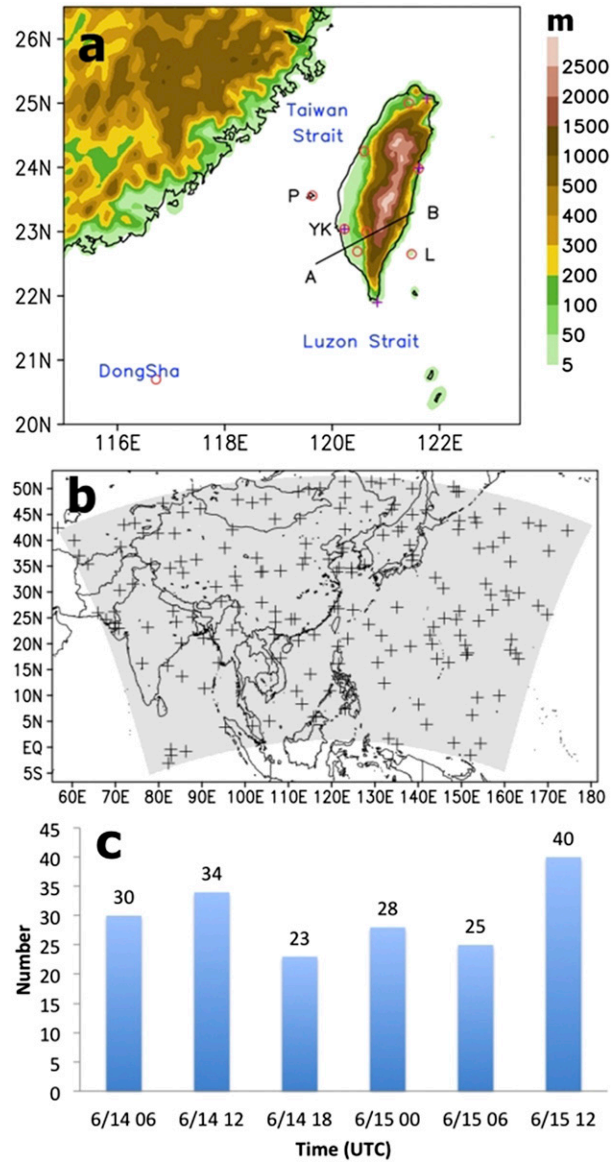

FIG. 1. (a) Terrain height (m) in color and locations (red circles) for nine rawinsonde sites over Taiwan and one upstream site (DongSha Island). The plus signs in purple are Doppler radar sites. The symbols "YK," "P," and "L" mark the location for the YongKang, Penghu, and Lyudao stations, respectively. Line AB is the cross section used for the depiction of interaction between the upstream southwesterly flow and cold pool over southwestern Taiwan. (b) The locations of 180 COSMIC GPS RO soundings assimilated by the cycling run during 0000 UTC 14 Jun–1200 UTC 15 Jun 2008. (c) The number of GPS RO soundings assimilated in each data assimilation cycle.

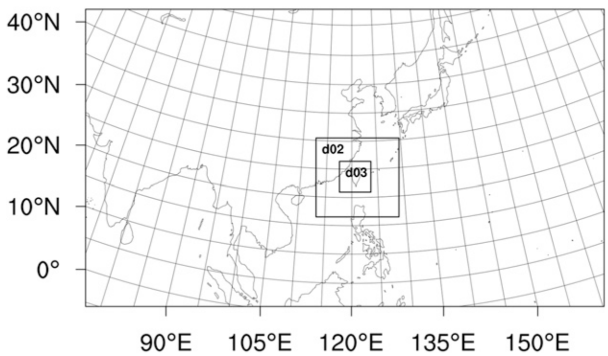

FIG. 2. The three nested domains of the WRF Model simulation with horizontal grid size of 27, 9, and 3 km, respectively.

convective showers toward the southwestern coast and extensive cloud cover over southwestern Taiwan, the cold pool persisted during the day with an offshore wind component along the coast (Tu et al. 2014). As a result, during 15–16 June, the rainfall distribution had a significant coastal maximum over southwestern Taiwan.

In Tu et al. (2014), the initial conditions for their regional 9-km domain and the island-scale domain (3 km) were interpolated from the National Centers for Environmental Prediction (NCEP) Final (FNL) analysis without modifications of the planetary boundary layer over southwestern Taiwan by the antecedent rains and small-scale features related to terrain and local winds. Furthermore, the NCEP FNL analysis used by Tu et al. (2014) and Wang et al. (2014a,b) does not include TiMREX observations. Yang et al. (2014) applied data assimilation to the outer domain to improve the large-scale conditions, especially moisture distribution, for the initial conditions and subsequent forecasts. They showed that assimilating the bending angle of the global positioning system (GPS) radio occultation (RO) soundings results in the deepening of the midtroposphere moist layer in the South China Sea and over southwestern Taiwan, which leads to a better rainfall forecast over the coastal region of southwestern Taiwan.

In this study, we apply a cycling run with data assimilation to all domains (e.g., outer domain and nest domains) to include TiMREX data, Global Telecommunications System (GTS) data, and refractivity from the Formosa Satellite Mission 3/Constellation Observing System for Meteorology, Ionosphere, and Climate (FORMOSAT-3/COSMIC, hereafter referred to as COSMIC) GPS RO soundings. In section 3, we demonstrate the improvements in model initial conditions (at 1200 UTC 15 June) through the cycling run (0000 UTC 14 June–1200 UTC 15 June) for real-time forecast including subsynoptic features (e.g., southwesterly monsoon flow and warm moisture tongue) in the outer domain (domain 1) and the cold pool from antecedent rains and its impact on orographic blocking in the high-resolution nested domains. In the meantime, for the outer model domain, we use a 36-h cycling run and bring in large-scale observational data to prevent model drift of the large-scale flow during the cycling run. In section 4, we demonstrate the impacts of the cycling run with data assimilation on subsynoptic and island-scale forecasts. In section 5, we conduct sensitivity tests to diagnose the effects of rain-evaporative cooling on the intensity and depth of the cold pool and degree of orographic blocking on the southwesterly flow over southwestern Taiwan. The impact of orographic effects on focusing coastal rainfall is also addressed based on model sensitivity tests.

2. Data and methodology

a. *Local and rainfall observations, GTS data, and YOTC analysis*

During TiMREX, there were 25 operational conventional surface weather stations, 9 rawinsonde stations including special TiMREX sites, and 4 operational Doppler radars (Fig. 1a) over the island of Taiwan. Additionally, soundings launched from DongSha Island (Fig. 1a) provided upstream conditions over the open ocean. Humidity, wind, temperature, and geopotential height from rawinsonde stations were corrected through a four-stage quality control (QC) procedure (Ciesielski et al. 2010). A correction, designed to remove the daytime dry bias resulting from solar heating of the humidity instrument, was applied to the Vaisala RS80 and Vaisala RS92 sondes. All types of sondes were corrected to the standard of the Vaisala RS92. See Ciesielski et al. (2010) for more details on quality control of sounding data. Rainfall accumulation maps over

TABLE 1. The experimental design for all model runs.

Expt name	Data assimilation cycling run (0000 UTC 14 Jun–1200 UTC 15 Jun)	Forecast run (1200 UTC 15 Jun–0000 UTC 17 Jun)
CTRL	No data assimilation cycling run	With cumulus parameterization and microphysics scheme
DA_ALL_DATA	DA run for all three domains; assimilate GTS, GPS RO, and TiMREX data	With cumulus parameterization and microphysics scheme
NEVP	As in DA_ALL_DATA run	No rain-evaporative cooling from microphysics scheme
NoT	DA for all three domains (with the island terrain removed)	As for the DA_ALL_DATA run, but with the island terrain removed

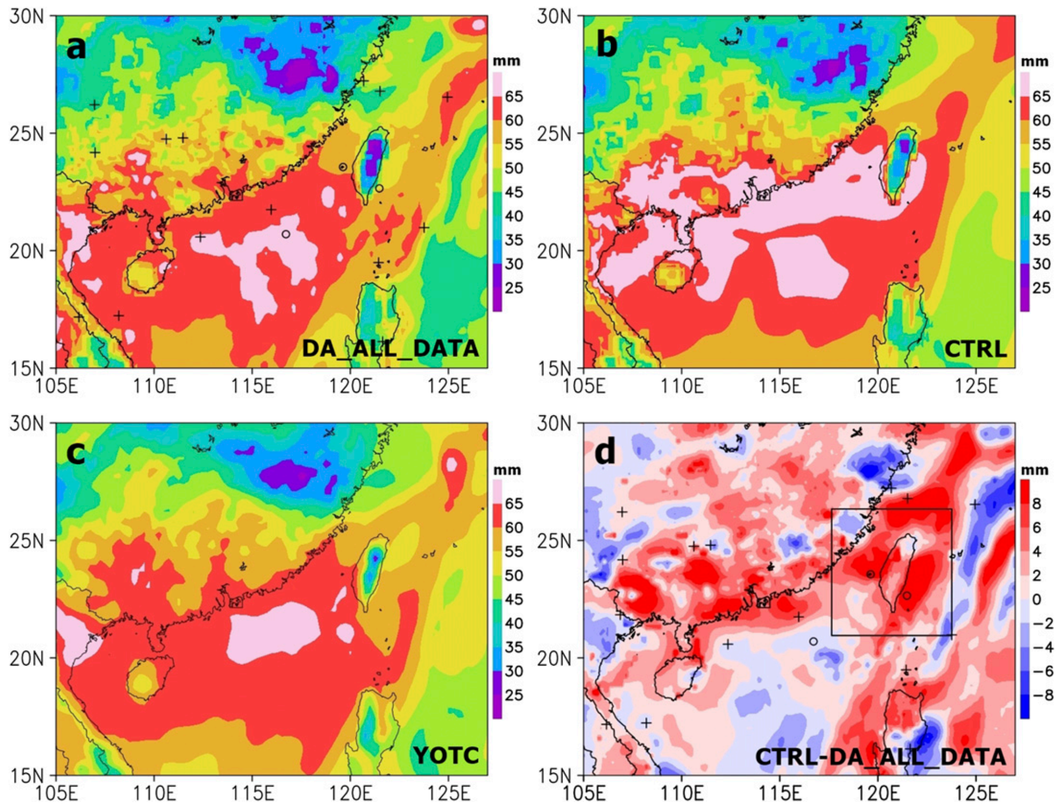

FIG. 3. The initial conditions over domain 1 at 1200 UTC 15 Jun 2008 after the cycling run. The locations of soundings and GPS RO refractivity profiles assimilated into the cycling run are indicated by circles and plus signs, respectively. (a) TPW (mm) for the DA_ALL_DATA run. (b) As in (a), but for the GFS analysis. (c) As in (a), but for the YOTC analysis. (d) Differences between CTRL and DA_ALL_DATA runs (CTRL − DA_ALL_DATA) for TPW (mm) at model initial time (1200 UTC 15 Jun).

the island are generated from 429 rainfall stations, which include conventional surface weather stations and the Automatic Rainfall and Meteorological Telemetry System (ARMTS) (Kerns et al. 2010). For a more detailed description of the TiMREX observational network see Tu et al. (2014).

The 30-min Climate Prediction Center morphing technique (CMORPH) (Joyce et al. 2004) precipitation data with an 8-km grid were also used to delineate rainfall distributions over the adjacent ocean. The CMORPH precipitation estimates are derived from passive microwave instruments (Advanced Microwave Sounding Unit-B and the Special Sensor Microwave Imager) on board the U.S. Defense Meteorological Satellite Program (DMSP) satellites (SSM/I) and National Oceanic and Atmospheric Administration (NOAA) polar-orbiting operational meteorological satellites (AMSU-B), and the Tropical Rainfall Measuring Mission (TRMM) Microwave Imager (TMI) on board the TRMM satellite (Joyce et al. 2004).

The GTS (Daley 1991) data include observations from manned and automated weather stations, pilots, ships, buoys, upper-air soundings, aircraft, profilers, the TIROS Operational Vertical Sounder (TOVS) temperature profile (SATEM), satellite-derived winds (SATOB), and Quick Scatterometer (QuikSCAT) ocean surface winds. The estimated observation errors for GTS data used by the Weather Research and Forecasting Model data assimilation (WRFDA) system (Skamarock et al. 2008) are given by NCEP (Rogers et al. 1996) and updated by the National Center for Atmospheric Research (NCAR) WRFDA team (http://www2.mmm.ucar.edu/wrf/users/wrfda/).

The European Centre for Medium-Range Weather Forecasts (ECMWF) Year of Tropical Convection (YOTC) (Moncrieff et al. 2012) analysis is used to delineate the subsynoptic weather patterns and compared with model output, including the moisture tongue and southwesterly flow. The YOTC gridded data have a 0.25° grid (http://apps.ecmwf.int/datasets/data/yotc-od/).

b. The GPS RO data

The GPS RO data are of high quality with a global coverage (e.g., Rocken et al. 1997; Hajj et al. 2004; Kuo et al. 2004, 2005; Wickert et al. 2004; Anthes 2011).

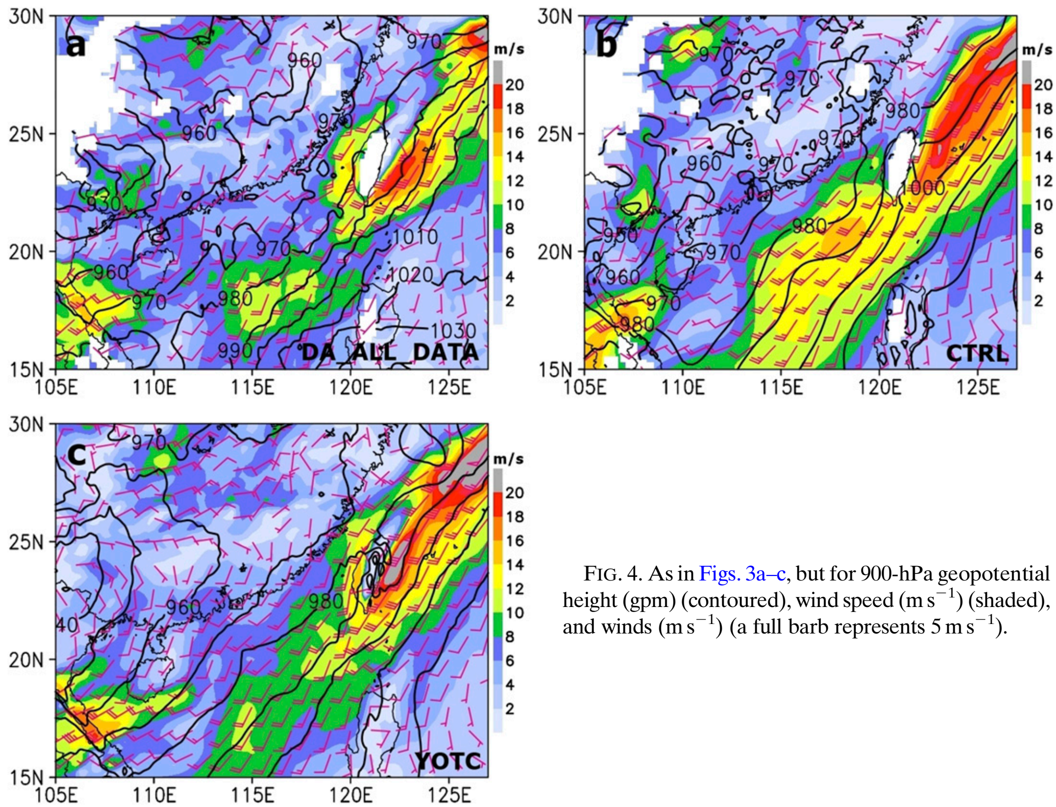

FIG. 4. As in Figs. 3a–c, but for 900-hPa geopotential height (gpm) (contoured), wind speed (m s^{-1}) (shaded), and winds (m s^{-1}) (a full barb represents 5 m s^{-1}).

There are numerous studies demonstrating the positive impact of improving model initial conditions through data assimilation of GPS RO data on numerical weather prediction (e.g., Kuo et al. 2000; Huang et al. 2005; Healy et al. 2007; Chen et al. 2009; Cucurull et al. 2013; Yang et al. 2014).

In this study, the GPS RO refractivity (N) data with a vertical interval ~200 m is used for data assimilation using the WRFDA system (Skamarock et al. 2008). The refractivity data are available at the COSMIC Data Analysis and Archive Center (CDAAC) (http://cdaac-www.cosmic.ucar.edu/). The refractivity N is a function of temperature T(K), pressure p (hPa), and water vapor pressure e (hPa) (Smith and Weintraub 1953):

$$N = 77.6\frac{P}{T} + 3.73 \times 10^5 \frac{e}{T^2}. \quad (1)$$

The observation error for the GPS refractivity data is about 2.5% near the surface at the equator and 1.5% at the pole regions. The error decreases with respect to height with a minimum of 0.3% above the 12-km level. The observational error of a RO refractivity profile located between the equator and pole is obtained from linear interpolation. A detailed description of the observation errors of GPS RO data can be found in Chen et al. (2011, 2014).

c. Model description and data assimilation

The Advanced Research version of the Weather Research and Forecasting (WRF-ARW, hereafter WRF) Model (Skamarock et al. 2008) uses the sigma (terrain following) hydrostatic-pressure vertical coordinate (Laprise 1992). Three model domains with two-way nesting are used with horizontal grids of 27, 9, and 3 km, respectively (Fig. 2). There are 45 sigma levels[1] from the surface to the 30-hPa level. The Rapid Radiative Transfer Model (RRTM) (Mlawer et al. 1997), Goddard shortwave (Chou and Suarez 1994) scheme, Noah land surface model (LSM) (Chen and Dudhia 2001), Yonsei University (YSU) planetary boundary layer scheme (Hong et al. 2006), and modified Kain–Fritsch cumulus parameterization scheme (Kain 2004) are used. The precipitation process in the model is represented by the grid-resolvable Goddard microphysics (Tao and Simpson 1993) with three classes of ice, including graupel. No cumulus parameterization is applied for the 3-km domain (domain 3). The precipitation

[1] The full sigma levels are 1.0, 0.995, 0.988, 0.98, 0.97, 0.96, 0.945, 0.93, 0.91, 0.89, 0.87, 0.85, 0.82, 0.79, 0.76, 0.73, 0.69, 0.65, 0.61, 0.57, 0.53, 0.49, 0.45, 0.41, 0.37, 0.34, 0.31, 0.28, 0.26, 0.24, 0.22, 0.2, 0.18, 0.16, 0.14, 0.12, 0.1, 0.082, 0.066, 0.052, 0.04, 0.03, 0.02, 0.01, and 0.000.

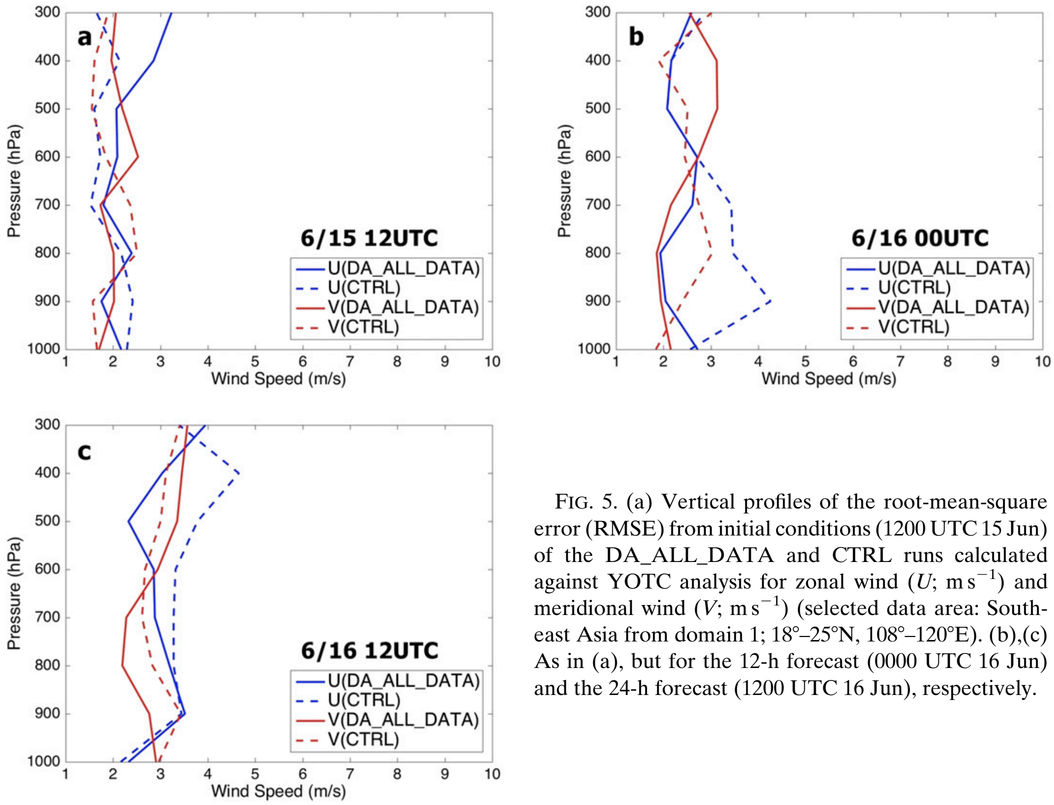

FIG. 5. (a) Vertical profiles of the root-mean-square error (RMSE) from initial conditions (1200 UTC 15 Jun) of the DA_ALL_DATA and CTRL runs calculated against YOTC analysis for zonal wind (U; m s^{-1}) and meridional wind (V; m s^{-1}) (selected data area: Southeast Asia from domain 1; 18°–25°N, 108°–120°E). (b),(c) As in (a), but for the 12-h forecast (0000 UTC 16 Jun) and the 24-h forecast (1200 UTC 16 Jun), respectively.

process and parameterization scheme used in this study are the same as those used by Hsiao et al. (2012). The surface layer uses the fifth-generation Pennsylvania State University–NCAR Mesoscale Model (MM5) similarity scheme with stability functions from Paulson (1970), Dyer and Hicks (1970), and Webb (1970). A 0.5° daily real-time global sea surface temperature (RTG_SST) analysis developed at the NCEP/Marine Modeling and Analysis Branch (MMAB) is used as the lower boundary condition over the ocean (Gemmill et al. 2007). The land use data over Taiwan, updated by the Central Weather Bureau (CWB), are used (Dr. J.-S. Hong 2011, personal communication).

The WRF three-dimensional variational (3DVAR) data assimilation system provides an analysis $\mathbf{x}^a$ via the minimization of a prescribed cost function $J(\mathbf{x})$ (Ide et al. 1997):

$$J(\mathbf{x}) = J_b(\mathbf{x}) + J_o(\mathbf{x}) = \frac{1}{2}(\mathbf{x} - \mathbf{x}^b)^{\mathrm{T}}\mathbf{B}^{-1}(\mathbf{x} - \mathbf{x}^b) + \frac{1}{2}(\mathbf{y} - \mathbf{y}^o)^{\mathrm{T}}(\mathbf{E} + \mathbf{F})^{-1}(\mathbf{y} - \mathbf{y}^o), \qquad (2)$$

where analysis $\mathbf{x} = \mathbf{x}^a$ represents the a posteriori minimum variance estimate of the true state of the atmosphere given two sources of a priori data: the background (first guess) $\mathbf{x}^b$ and observations $\mathbf{y}^o$ (Lorenc 1986). The analysis fit to individual data points is weighted by estimates of their errors. In Eq. (2), $\mathbf{B}$, $\mathbf{E}$, and $\mathbf{F}$ are the background, observation, and representativeness error covariance matrices, respectively. Representativeness error is an estimate of inaccuracies introduced in the observation operator H used to transform the grid point analysis $\mathbf{x}$ to observation space $\mathbf{y} = H(\mathbf{x})$. The analysis increments $\mathbf{x}'$ are added to the first guess $\mathbf{x}^b$ to provide an updated analysis, an optimal estimate of the true atmospheric state (Barker et al. 2004).

The experimental design for all model runs is listed in Table 1. For the DA_ALL_DATA run, we perform a WRF 3DVAR cycling run from 0000 UTC 14 June to 1200 UTC 15 June by assimilating TiMREX soundings,

TABLE 2. Root-mean-square error of domain 1 TPW (mm) over the oceanic area covered by 18°–25°N, 108°–120°E from the initial conditions (1200 UTC 15 Jun), and 12-h and 24-h forecasts of the DA_ALL_DATA and CTRL runs calculated against YOTC analysis.

RMSE	DA_ALL_DATA	CTRL
1200 UTC 15 Jun	2.53	2.78
0000 UTC 16 Jun	2.57	2.59
1200 UTC 16 Jun	2.63	2.86

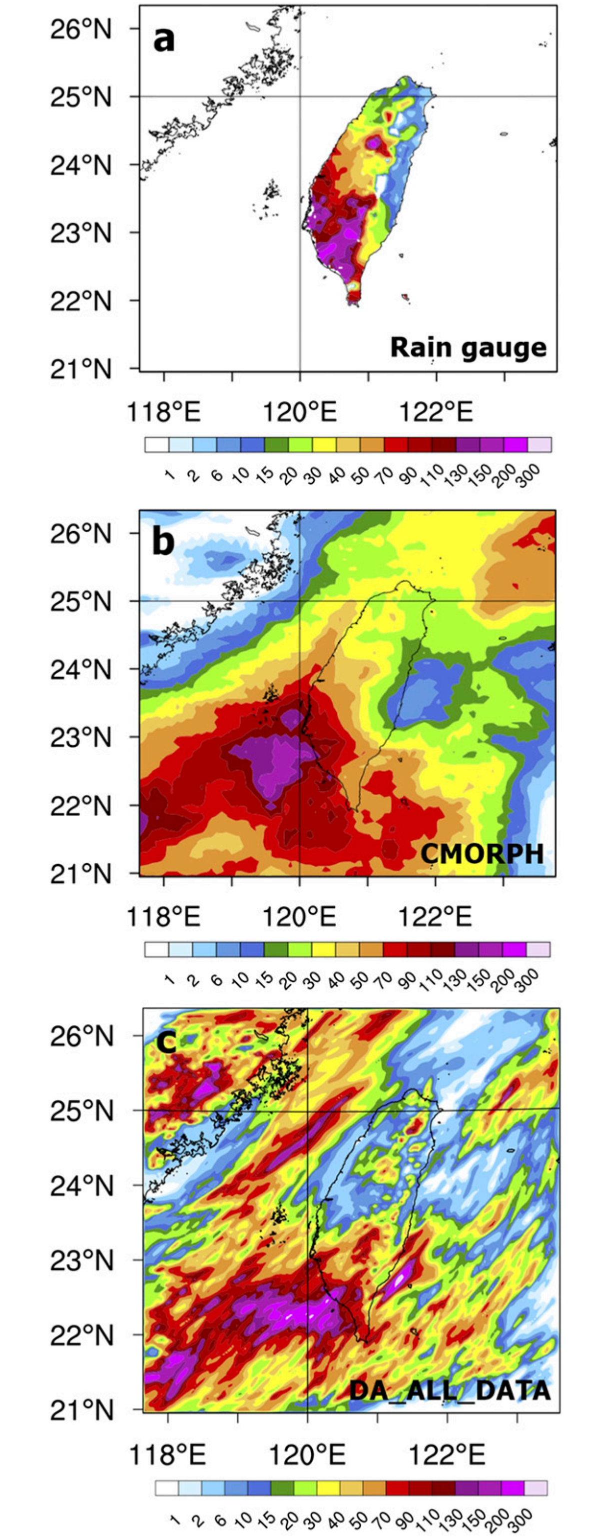

FIG. 6. Total rainfall accumulation (mm) during 0000 UTC 14 Jun–1200 UTC 15 Jun from (a) rain gauge observations, (b) CMORPH data (8-km resolution), and (c) the DA_ALL_DATA run (domain 3).

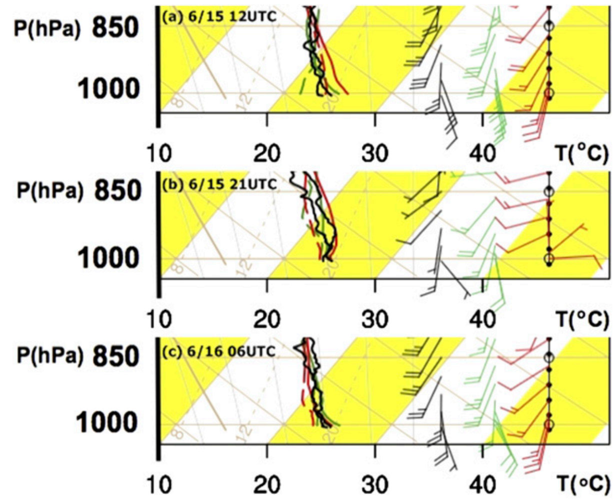

FIG. 7. (a) The observed sounding (black) and simulated soundings from domain 3 at the model initial time (1200 UTC 15 Jun) from the DA_ALL_DATA (green) and CTRL runs (red) for the YongKang station. Winds ($m\,s^{-1}$) (a full barb represents $5\,m\,s^{-1}$). (b),(c) As in (a), but for model forecasts at 2100 UTC 15 Jun and 0600 UTC 16 Jun, respectively.

GPS RO refractivity profiles, and GTS data every 6 h within a ±3-h time window using the WRFDA system to provide better initial conditions at 1200 UTC 15 June for the regional and nested domains. Lateral boundary conditions during the subsequent forecast are provided by the GFS forecast. For domain 1, from 0000 UTC 14 June to 1200 UTC 15 June 2008, 180 COSMIC GPS RO refractivity profiles (Fig. 1); 18 TiMREX soundings from Dongsha, Penghu, and Lyudao stations (Fig. 1a); and the GTS data (excluding observations from land based stations over Taiwan) are assimilated. For domains 2 and 3, in addition to GPS RO refractivity profiles, all 54 available soundings from TiMREX stations and all GTS data are assimilated. The control variables with option 5 (CV5) statistical background error covariance matrix (Skamarock et al. 2008) are used for data assimilation. The CV5 background error statistics (BES) is computed according to the method described by Parrish and Derber (1992). The CV5 BES is estimated using the differences between 12- and 24-h WRF forecasts over the month of June 2008, which includes this heavy rainfall case. The initial conditions at 1200 UTC 15 June have finescale details for the regional and nested domains that are consistent in both space and time through the cycling run with data assimilation that include TiMREX, GPS RO, and GTS data prior to 1200 UTC 15 June. Thus, the orographic effects and effects of prior weather systems (e.g., rain-evaporative cooling over southwestern Taiwan) in the high-resolution domains are included in the model initial conditions and subsequent forecasts.

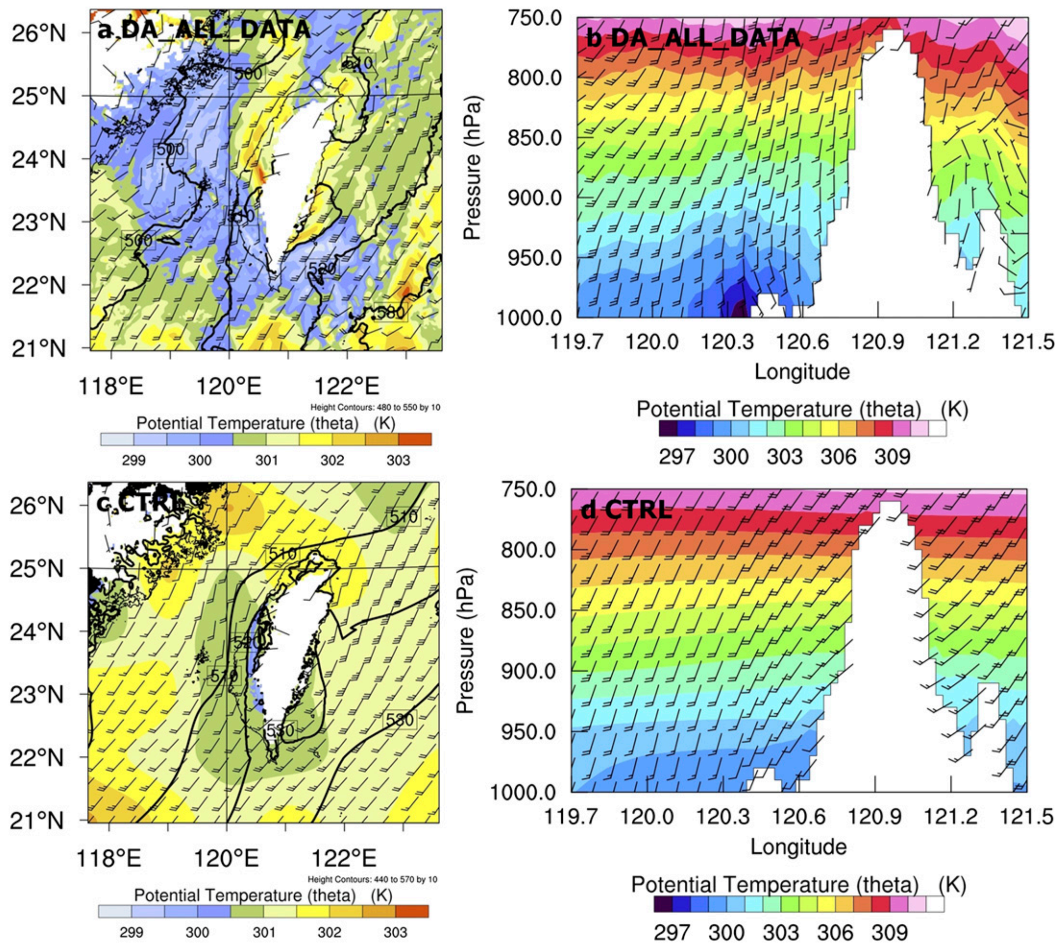

FIG. 8. Model initial conditions for domain 3 at 1200 UTC 15 Jun. (a) 950-hPa potential temperature (K) (shaded), geopotential height (gpm) (contoured), and winds (m s^{-1}) (a full barb represents 5 m s^{-1}), and (b) vertical cross sections of potential temperature (K) (shaded) and winds (m s^{-1}) (a full barb represents 5 m s^{-1}) along line AB in Fig. 1a for the DA_ALL_DATA run. (c),(d) As in (a),(b), but for the GFS analysis.

For the control run (CTRL), the initial conditions at 1200 UTC 15 June in the regional and nested domains are interpolated from the GFS analysis, which has a relatively coarse grid on the order of 1°. Note that the TiMREX soundings did not enter the NCEP GFS in real time. After the initial model spinup period (~6 h) (Yeh and Chen 2003), orographic effects will be generated in the high-resolution domain but without the effects of prior weather systems (e.g., rain-evaporative cooling). We conduct two model sensitivity tests to investigate the effects of rain-evaporative cooling and terrain by turning off rain evaporation (NEVP run) and removing the terrain (NoT run) in the model forecasts, respectively. There are two different ways to perform no rain-evaporative cooling experiments. One way is to allow the raindrops to evaporate without the feedback of latent cooling in the thermodynamic equation (Yang and Houze 1995). The other way is to completely remove the raindrop-evaporation process and associated latent cooling effect in the microphysical parameterization (Zhu and Zhang 2006; Tao et al. 2013). In this study, we use the second method by turning off raindrop evaporation completely.

3. Improvements in model initial conditions with data assimilation through a 36-h cycling run

a. *A moisture tongue over the South China Sea and the southwesterly monsoon flow*

At 1200 UTC 15 June, the moisture tongue in the GFS analysis extends from the southeast coast of China eastward to the Taiwan area (Fig. 3b), which is different from the YOTC analysis that has a moisture tongue over the northern South China Sea (Fig. 3c). In contrast to the GFS analysis, the moisture tongue over the northern

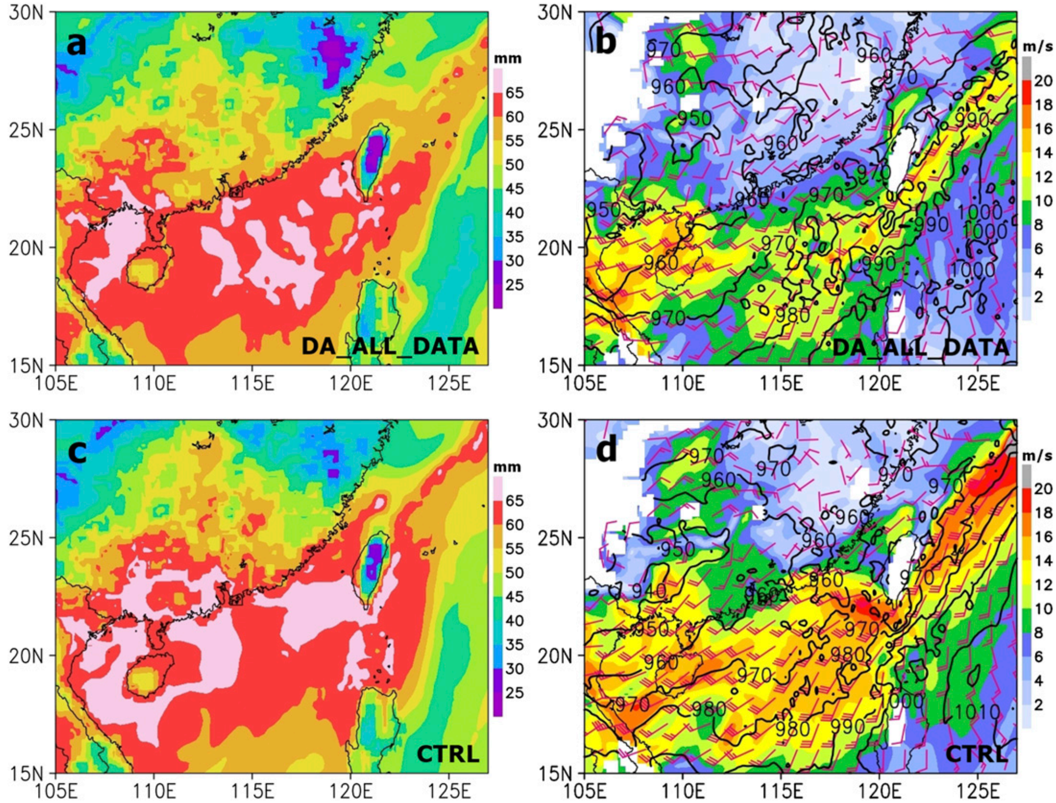

FIG. 9. Model forecasts at 2100 UTC 15 Jun for domain 1 of the DA_ALL_DATA run. (a) TPW (mm, shaded) and (b) 900-hPa winds (m s^{-1}) (a full barb represents 5 m s^{-1}) and geopotential height (gpm, contoured). (c),(d) As in (a),(b), but for the CTRL run.

South China Sea is well defined in the DA_ALL_DATA run with lower moisture over the Taiwan area (Fig. 3a), consistent with the YOTC analysis (Fig. 3c). It is apparent that the 36-h cycling run with data assimilation has a positive impact in delineating the moisture tongue over the northern South China Sea. Without assimilating GTS data, GPS RO refractivity profiles, and 18 TiMREX soundings from three island stations, TPW is lower over the northern South China Sea and higher over southeastern China extending eastward to the ocean off the eastern Taiwan coast (Fig. 3d). At the 900-hPa level, the south-southwesterly monsoon flow off southwestern Taiwan (Fig. 4a) is well simulated in the DA_ALL_DATA run, consistent with the YOTC analysis (Fig. 4c). In contrast, for the GFS analysis used in the CTRL run, the southwesterly monsoon flow off the southwestern Taiwan coast is stronger with a relatively large westerly wind component (Fig. 4b) as compared to both the DA_ALL_DATA run and the YOTC data.

At the model initial time, the vertical profiles of the root-mean-square error (RMSE) for the horizontal winds and TPW were calculated against YOTC analysis using data from domain 1 for the area covered by 18°–25°N, 108°–120°E for both the DA_ALL_DATA and CTRL runs. For both components of the horizontal winds, the RMSE at the model initial time for both runs is small (Fig. 5). However, at the 900-hPa level, the RMSE of zonal wind is larger for the CTRL run than the DA_ALL_DATA run (Fig. 5a) due to the relatively stronger southwesterly flow upstream of Taiwan (Fig. 4). During model integration, the forecast error of horizontal winds increases (Fig. 5). The RMSE of the horizontal winds for the CTRL run (without data assimilation) are larger than the DA_ALL_DATA run at low levels during the heavy rainfall period (Figs. 5b and 5c). The RMSE of the TPW for the CTRL run is larger than the DA_ALL_DATA run at the model initial time and during the model forecasts (Table 2).

b. *The cold pool over southwestern Taiwan due to evaporative cooling from antecedent rains*

From 0000 UTC 14 June to 1200 UTC 15 June, heavy rainfall occurred over southwestern Taiwan (Figs. 6a and 6b) during the passage of a squall line. At the YongKang station (Fig. 1a) on the southwestern Taiwan coast, the temperature below the 850-hPa level at

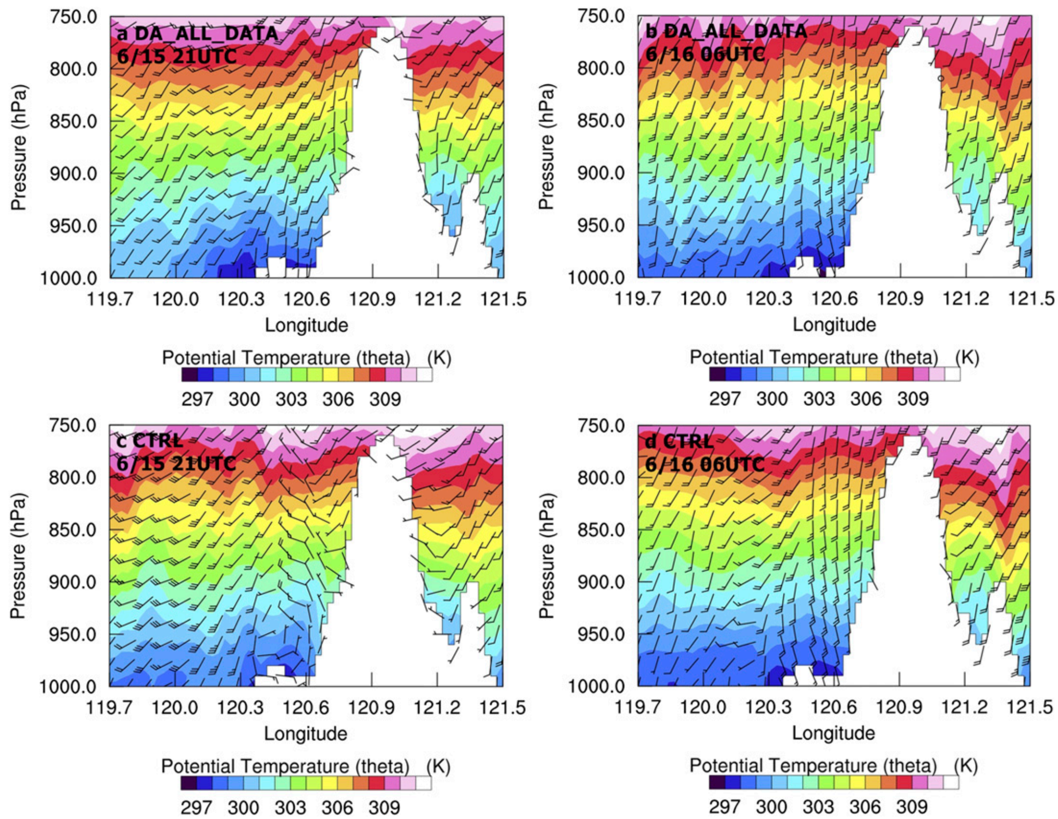

FIG. 10. The cross section of potential temperature (K) and winds (m s^{-1}) (a full barb represents 5 m s^{-1}) along line AB in Fig. 1a for the DA_ALL_DATA run at (a) 2100 UTC 15 Jun and (b) 0600 UTC 16 Jun. (c),(d) As in (a),(b), but for the CTRL run.

the model initial time (1200 UTC 15 June) of the DA_ALL_DATA run (green line) is colder (~1°–2°C) than the initial conditions used by the CTRL run (red line) (Fig. 7a). For the DA_ALL_DATA run, at the model initial time, the simulated YongKang sounding (green line) is in good agreement with observations (black line). The observed southeasterly winds within the cold pool (black wind barbs) are also reproduced (green wind barbs) (Fig. 7a). In contrast, for the CTRL run, the low-level cold pool and the offshore wind component are not simulated at the YongKang station (red wind barbs) (Fig. 7a).

At the 950-hPa level, the air temperature over southwestern Taiwan and off the southwestern Taiwan coast at the model initial time for the DA_ALL_DATA run is colder (~2 K) than the GFS analysis used in the CTRL run (Figs. 8a and 8c) because the effects of rain evaporation from antecedent rains are included in the DA_ALL_DATA run (Fig. 6). Furthermore, with the presence of the cold pool over southwestern Taiwan and the adjacent ocean, the incoming southwesterly flow is deflected upstream and becomes south-southeasterly over southwestern Taiwan (Fig. 8a) as a result of blocking.

From the vertical cross section (line AB in Fig. 1a) of the potential temperature and winds, it is obvious that at the model initial time of the DA_ALL_DATA run the cold pool extends vertically upward to above the 900-hPa level with a southerly flow parallel to the Central Mountain Range (CMR) over southwestern Taiwan (Fig. 8b), as found in Xu et al. (2012) and Tu et al. (2014). In contrast, the cold pool and the effects of blocking are not clearly evident (Figs. 8c and 8d) in the initial conditions used in the CTRL run. Furthermore, in the initial conditions of the CTRL run, the southwesterly flow prevails over southwestern Taiwan with a large westerly wind component impinging on CMR (Figs. 8c and 8d). In contrast, low-level winds over southwestern Taiwan simulated in the DA_ALL_DATA run have a slight easterly wind component due to the presence of the cold pool (Fig. 8b). Above the cold pool, winds over southwestern Taiwan are southerly in the DA_ALL_DATA run as a result of orographic blocking (Fig. 8b).

It is evident that the boundary layer structure over southwestern Taiwan in the DA_ALL_DATA run is affected by rain-evaporative cooling of the antecedent rains during 0000 UTC 14 June–1200 UTC 15 June

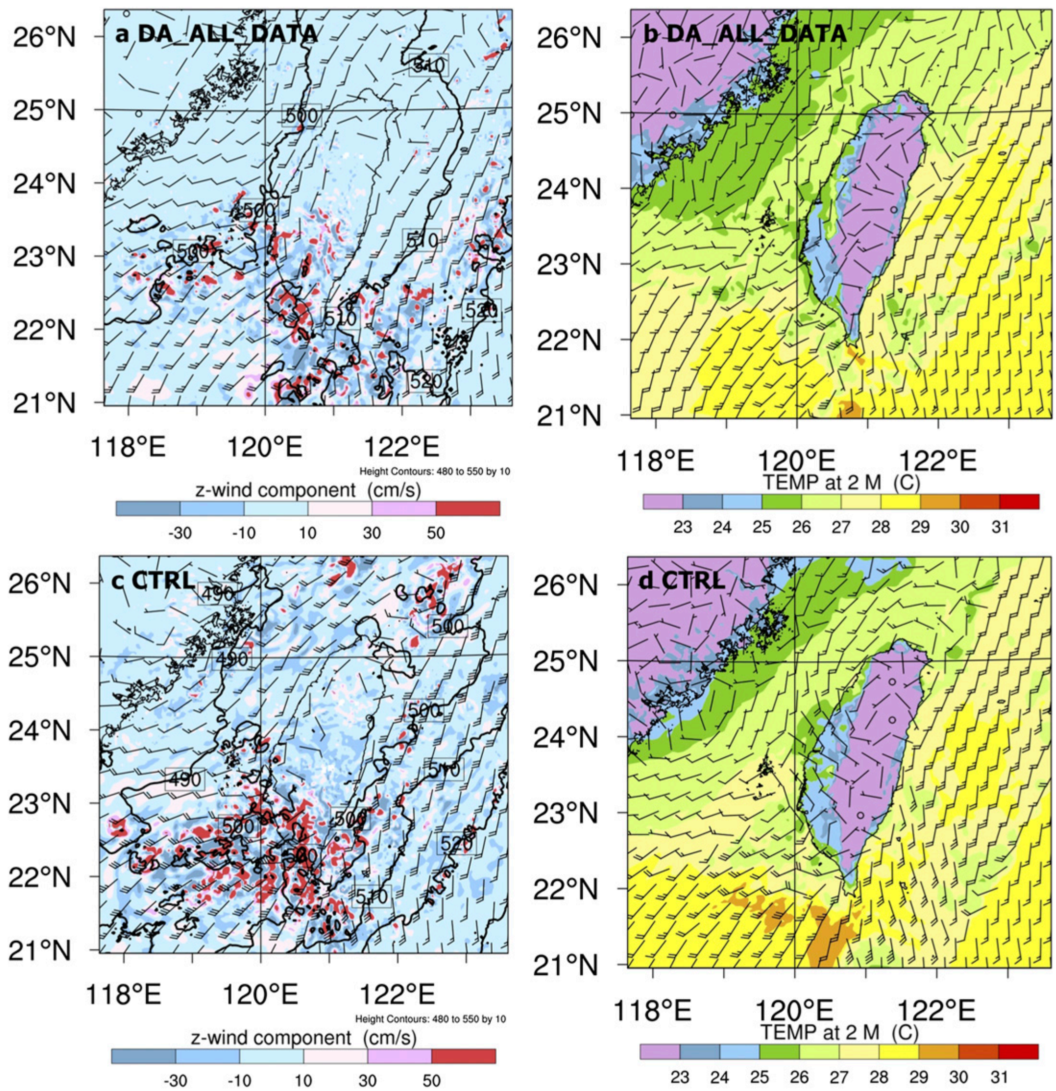

FIG. 11. Model forecasts for domain 3 valid at 2100 UTC 15 Jun. (a) The 950-hPa geopotential height (gpm) (contoured) and winds (m s^{-1}) (a full barb represents 5 m s^{-1}), and 700-hPa vertical velocity (cm s^{-1}); and (b) 2-m temperature (°C) and 10-m winds (m s^{-1}) (a full barb represents 5 m s^{-1}) for the DA_ALL_DATA run. (c),(d) As in (a),(b), but for the CTRL run.

and the effects of blocking due to the presence of the cold pool and island terrain. For the CTRL run, however, neither the effects of rain evaporation nor the effects of blocking are included in the model initial conditions.

4. Impacts of data assimilation with a cycling run on subsynoptic and island-scale forecasts

a. *Nighttime flow regime and rainfall*

At 2100 UTC 15 June (0500 LT 16 June), the low-level south-southwesterly monsoon flow prevails upstream of Taiwan in the DA_ALL_DATA run (Fig. 9b) bringing in abundant moisture to southwest Taiwan (Fig. 9a). The predicted low-level cold pool extends from southwestern Taiwan to the adjacent ocean (Fig. 10a). With the presence of the cold pool, the airflow turns from southwesterly to southerly over southwestern Taiwan in agreement with sounding observations (Figs. 7b and 10a). At the surface, with combined nocturnal cooling and rain-evaporative cooling, an offshore flow component is predicted over the coastal area (Fig. 11b). The incoming south-southwesterly monsoon flow decelerates off the southwestern coast (Fig. 11a). Localized upward motion is predicted over the southwest coast and adjacent ocean (Fig. 11a) with the rainfall maximum over

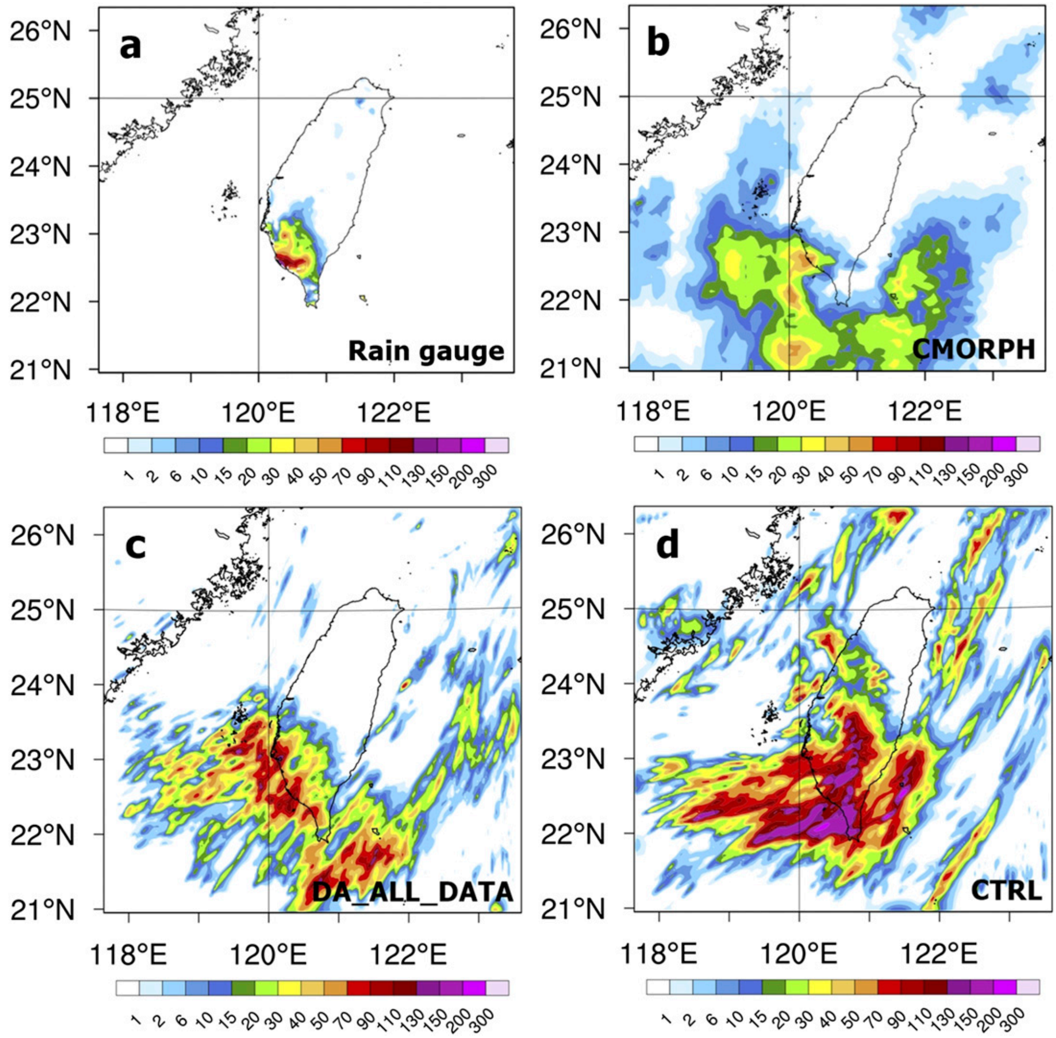

FIG. 12. Total rainfall accumulation (mm) during 1600 UTC 15 Jun–0000 UTC 16 Jun from (a) rain gauge observations, (b) CMORPH data (8-km resolution), (c) DA_ALL_DATA, and (d) CTRL runs (domain 3).

the coastal area and offshore (Fig. 12c) in agreement with observations (Figs. 12a and 12b).

In the CTRL run, because the incoming moist southwesterly monsoon flow has a relatively large westerly wind component (Figs. 9c and 9d) impinging on the CMR (Fig. 10c), widespread orographic precipitation is predicted along the windward side of the CMR (Fig. 12d) due to orographic lifting there (Fig. 11c). A cold pool is predicted in the planetary boundary layer over southwestern Taiwan and the adjacent ocean as a result of combined rain-evaporative cooling and nocturnal cooling (Fig. 10c). Winds over the island are relatively weak with an offshore flow wind component near the surface within the cold planetary boundary layer (Figs. 10c and 11d). On the west-southwestern windward side, the convergence occurs between the incoming southwesterly monsoon flow and relatively weak winds over land with an offshore wind component (Fig. 11d). In addition, the 490-m geopotential height contour associated with the early summer monsoon trough over southeastern China extends farther eastward over the Taiwan Strait with a relatively larger westerly wind component over the southern Taiwan Strait with significant rising motion off the southwestern coast (Figs. 11c and 11d) as compared to the DA_ALL_DATA run (Figs. 11a and 11b). As a result, in addition to orographic precipitation on the windward side of CMR, considerable rainfall is predicted offshore over the southern Taiwan Strait (Fig. 12d). For the DA_ALL_DATA run, the cold pool along the southwestern coast and adjacent coastal areas is already present in the model initial conditions that affect the subsequent forecasts. In contrast, the cold pool is produced during the model forecast in the CTRL run due to significant orographic precipitation on the windward side

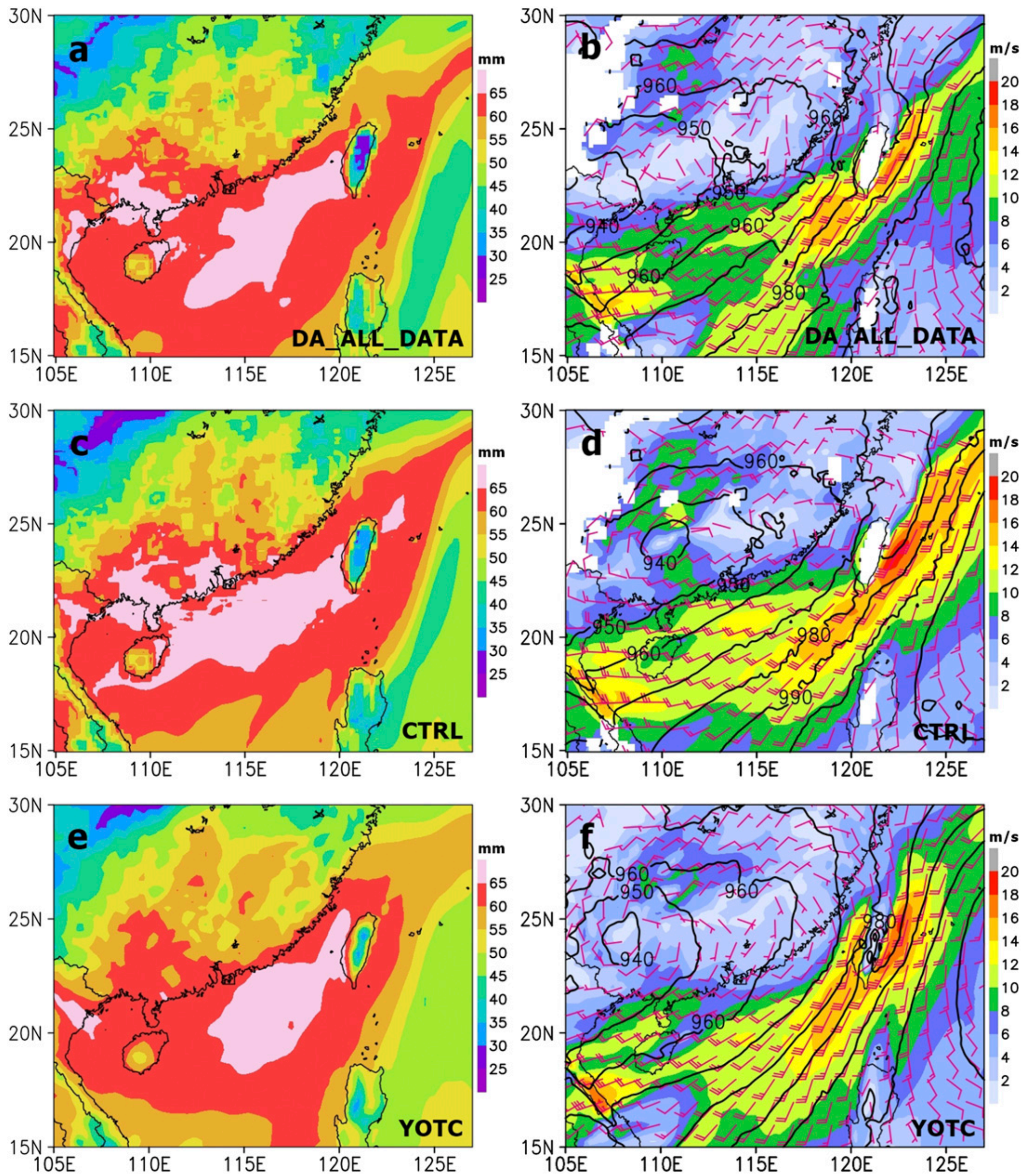

FIG. 13. Model forecasts averaged during 0000–1200 UTC 16 Jun for domain 1 of the DA_ALL_DATA run. (a) TPW (mm) (shaded) and (b) 900-hPa winds (m s^{-1}) (a full barb represents 5 m s^{-1}), and geopotential height (gpm) (contoured). (c),(d) As in (a),(b), but for the CTRL run. (e),(f) As in (a),(b), but for the YOTC analysis.

of CMR and the rainfall offshore. It is shallower over the coastal area but extends farther offshore with a larger horizontal extent (Fig. 10c) as compared to the DA_ALL_DATA (Fig. 10a). The larger horizontal extent of the cold pool in the CTRL run is related to much higher simulated rainfall over the ocean (Figs. 12c and 12d).

b. Daytime flow regimes and rainfall

During 0000–1200 UTC (0800–2000 LT) 16 June, in the CTRL run, the axis of the low-level southwesterly flow upstream of southwestern Taiwan shifts eastward with a slightly larger westerly wind component over the southern Taiwan Strait as compared to the DA_ALL_DATA run and the YOTC analysis (Figs. 13b,d,f). This is related to the fact that the simulated early summer monsoon trough over southeastern China extends slightly eastward toward the Taiwan Strait as compared to the DA_ALL_DATA run and YOTC analysis. Note that at 0600 UTC 16 June in the high-resolution domain, the 490-m geopotential height contour is slightly east of

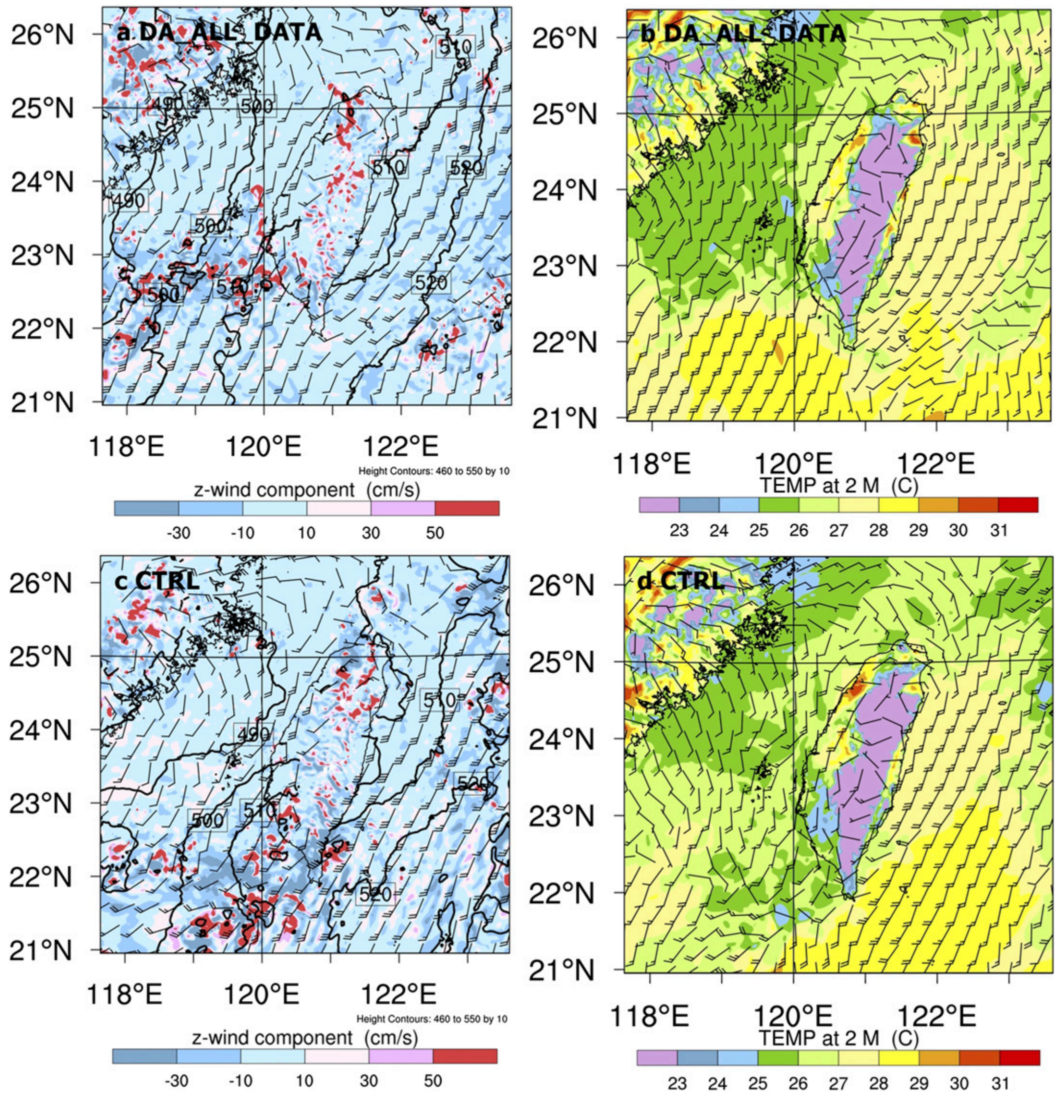

FIG. 14. As in Fig. 11, but for 0600 UTC 16 Jun.

118°E in the DA_ALL_DATA run (Fig. 14a) but extends eastward to the central Taiwan coast in the CTRL run (Fig. 14c). A moisture tongue over the northern South China Sea is simulated in the CTRL run consistent with the DA_ALL_DATA run and YOTC analysis (Figs. 13a,c,e). The predicted island wake of the southwesterly flow is off the northern Taiwan coast in both the DA_ALL_DATA and CTRL runs (Figs. 13b and 13d) in agreement with YOTC analysis (Fig. 13f).

During the daytime of 16 June, heavy rainfall occurs over southwestern Taiwan with a rainfall maximum over the coastal area (Fig. 15a). The CMORPH rainfall data also show heavy rainfall off the southwestern Taiwan coast (Fig. 15b). At 0600 UTC (1400 LT) 16 June, the DA_ALL_DATA run predicts a cold pool in the boundary layer over southwestern Taiwan (Fig. 10b) with decelerating incoming flow (Fig. 14a). The coastal rainfall related to the convergence of the offshore flow and decelerating southwesterly flow (Fig. 14b) is successfully predicted in the DA_ALL_DATA run (Fig. 15c). Over southwestern Taiwan, with the low-level flow parallel to the orientation of CMR (Fig. 10b), orographic lifting is almost absent (Fig. 14a) in the DA_ALL_DATA run, which is in agreement with Tu et al. (2014). As a result, heavy rain showers diminish (Fig. 15c) as they drift inland above the cold pool.

During the daytime of 16 June, heavy rainfall occurs over southwestern Taiwan in the CTRL run (Fig. 15d) due to rising motions over the southwestern Taiwan coast (Fig. 14c). With the eastward extension of the early summer monsoon trough, the overall rainfall pattern shifts southeastward with higher rainfall amounts (Fig. 15d) as

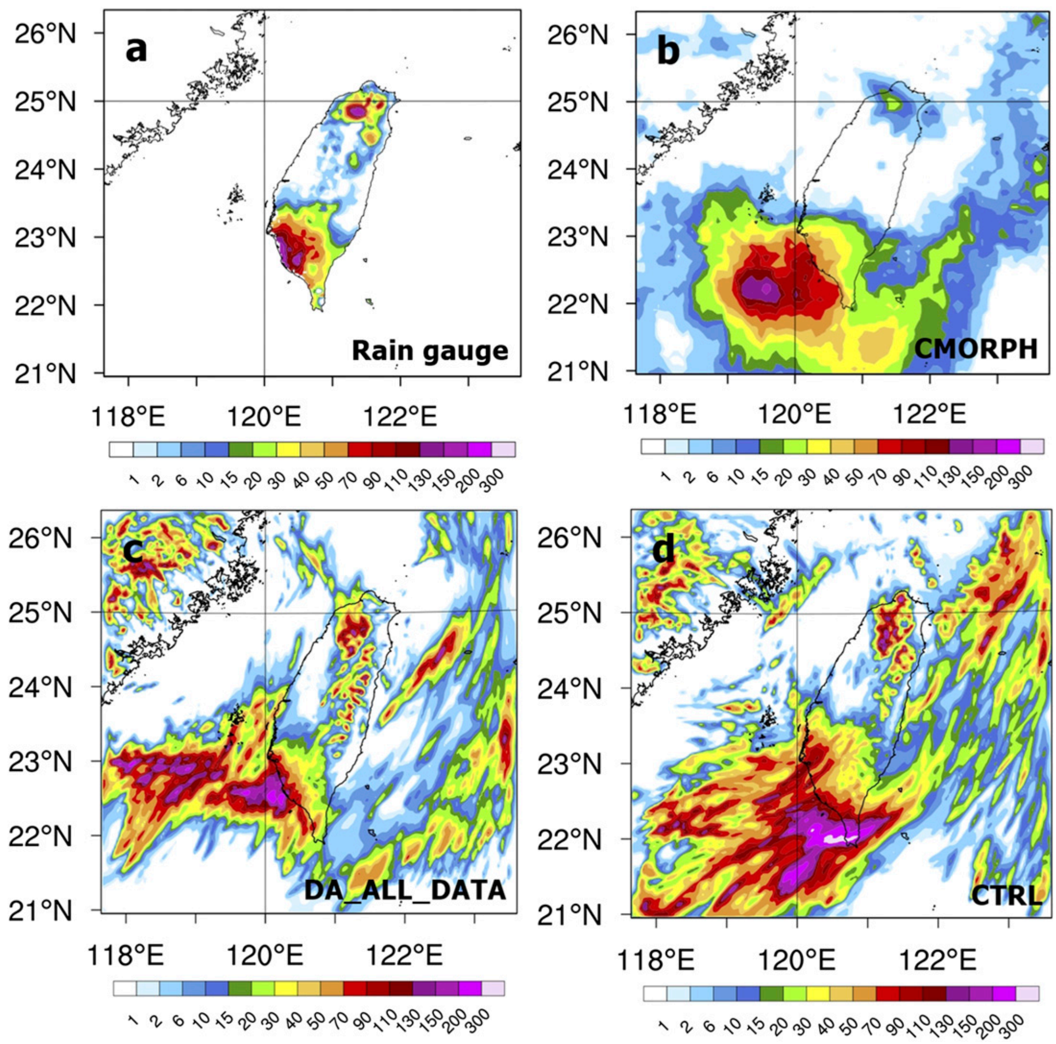

FIG. 15. Total rainfall accumulation (mm) during 0000–1000 UTC 16 Jun from (a) rain gauge observations, (b) CMORPH data (8-km resolution), (c) DA_ALL_DATA, and (d) CTRL runs (domain 3).

compared to the DA_ALL_DATA run (Fig. 15c). The low-level air temperature off the southwestern coast is slightly lower in the CTRL run (Fig. 14d) as compared to the DA_ALL_DATA run (Fig. 14b) due to rain-evaporative cooling there. As will be shown later based on the model sensitivity test without terrain (NoT), the rainfall production is related to large-scale process in addition to local effects. Nevertheless, with the presence of a cold pool offshore in the CTRL run (Fig. 10d), the predicted rainfall over southwestern Taiwan diminishes inland with higher rainfall along the coast than on the windward side of the CMR (Fig. 15d). In addition to rainfall in the coastal areas, significant precipitation is predicted over the southern tip of Taiwan.

In both the DA_ALL_DATA and CTRL runs, under relatively weak winds in the wake zone over northern Taiwan, the development of afternoon sea-breeze/upslope flow there in response to relatively cold sea surface temperature (SST) offshore and solar heating over land (Tu et al. 2014) is well predicted (Figs. 14b and 14d). As a result, heavy afternoon local showers over northern Taiwan are well predicted in the DA_ALL_DATA and CTRL runs (Fig. 15).

c. Postrainfall period

During 1800 UTC 16 June–0000 UTC 17 June, as the western Pacific subtropical high (WPSH) extended westward, Taiwan was under the influence of a WPSH with drier conditions aloft (Tu et al. 2014). As a result, heavy localized rainfall diminished over Taiwan (Figs. 16a and 16b). In both the DA_ALL_DATA and CTRL runs, the termination of heavy rainfall over Taiwan during this

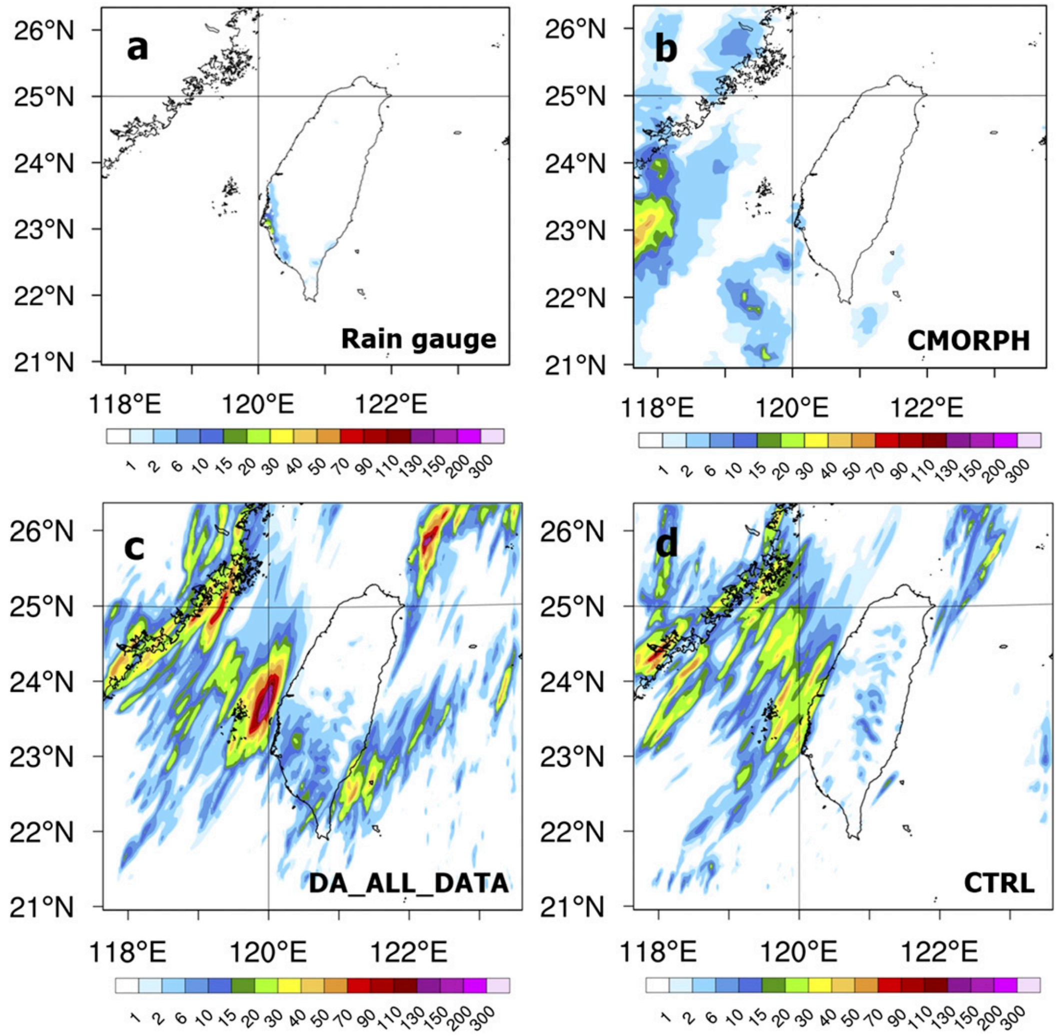

FIG. 16. Total rainfall accumulation (mm) during 1800 UTC 16 Jun–0000 UTC 17 Jun from (a) rain gauge observations, (b) CMORPH data (8-km resolution), (c) DA_ALL_DATA, and (d) CTRL runs (domain 3).

period is well predicted (Fig. 16). It is apparent that the synoptic flow has significant influence on the occurrence of this heavy rainfall event whereas the orographic effects and rain evaporation are important in determining the location of heavy precipitation.

In the next section, we will investigate the impacts of rain evaporation on model forecasts by turning off rain evaporation during time integration starting from the same initial conditions as the DA_ALL_DATA run. We will also investigate the impact of the island terrain on model forecasts.

5. Effects of rain-evaporative cooling and terrain

a. *Effects of rain-evaporative cooling*

When rain evaporation is turned off during model integration, the cold pool gradually disappears. In the NEVP run, at 2100 UTC 15 June (0500 LT 16 June) the south-southwesterly monsoon flow prevails over southwestern Taiwan with a relatively warm boundary layer (Figs. 17a and 18a) as compared to the DA_ALL_DATA run (Fig. 10a). The surface flow over the island is dominated by weak downslope/offshore winds (Fig. 18b) as a result of nocturnal cooling at the surface. The decelerating incoming flow converges with the weak south-southeasterly winds along the coast (Fig. 18b). Localized rainfall is simulated along the southwestern coast (Fig. 19a) where the incoming southwesterly flow encounters the south-southeasterly flow over land (Fig. 18b). Above the surface, winds are deflected by the terrain and become southerlies over southwestern Taiwan (Figs. 17a and 18a). Over southwestern Taiwan, without the presence of cold pool over coastal waters, the rainfall maximum in the NEVP run is simulated over the coastal area (Fig. 19a).

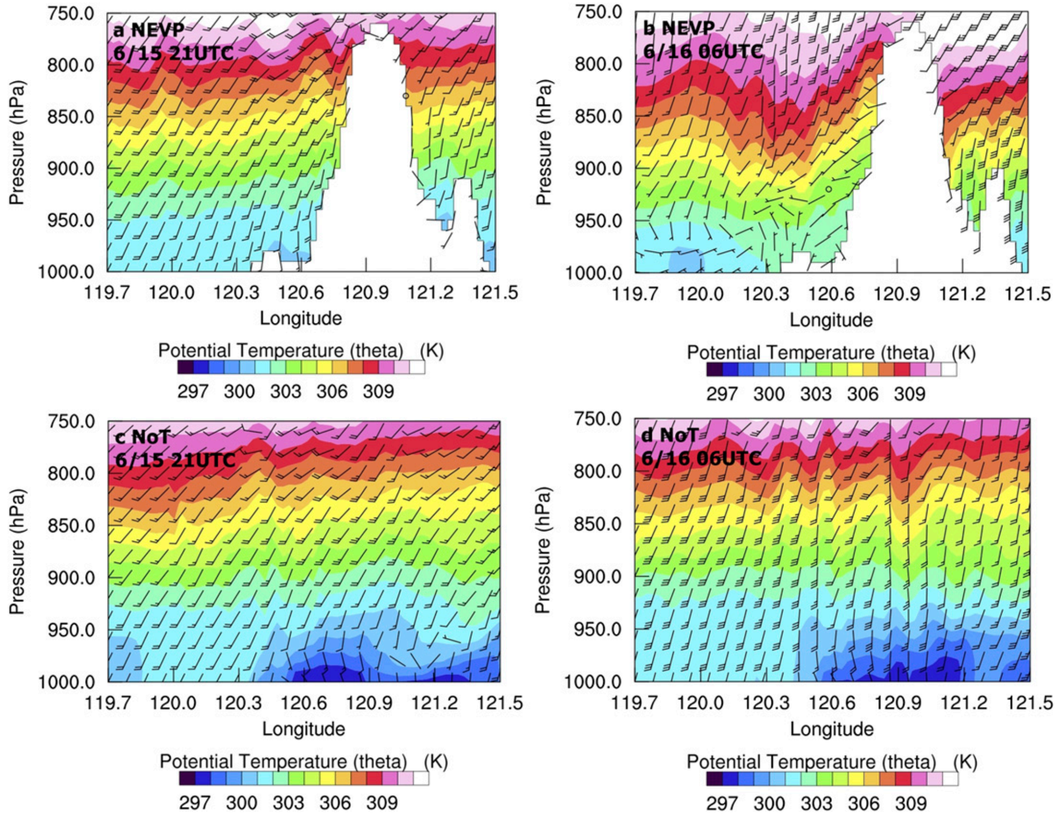

FIG. 17. Vertical cross sections of potential temperature (K) and winds (m s^{-1}) (a full barb represents 5 m s^{-1}) along line AB in Fig. 1a for the NEVP run at (a) 2100 UTC 15 Jun and (b) 0600 UTC 16 Jun. (c),(d) As in (a),(b), but for the NoT run.

Without rain-evaporative cooling during model integration, during the daytime of 16 June the early summer monsoon trough along the southeastern coast of China expands eastward with weaker winds over west-southwestern Taiwan (Fig. 20a) as compared to the DA_ALL_DATA run (Fig. 13b). At 0600 UTC (1400 LT) 16 June, the 500-gpm geopotential height contour at the 950-hPa level in the NEVP run extends to the eastern side of central-northern Taiwan (Fig. 21a) but is within the Taiwan Strait in the DA_ALL_DATA run (Fig. 14a). Zhu and Zhang (2006) showed that without evaporation of rain and cloud water, the minimum central pressure of Hurricane Bonnie is 10–15 hPa lower than with rain evaporation after an 18-h time integration. Thus, in the NEVP run, with relatively weak winds over the ocean off the southwestern coast and the absence of cold pool, upslope flow prevails over southwestern Taiwan in the afternoon hours (Figs. 17b and 21b). Over west-northwestern Taiwan, with solar heating over land and cold SST over the surrounding ocean, onshore/sea-breeze flow (Fig. 21b) prevails under weak wind conditions. Widespread heavy precipitation is predicted off the southwestern coast and over southern Taiwan with scattered heavy showers over northern Taiwan and along the eastern coast (Fig. 19b).

b. Effects of terrain

In the NoT run, the Taiwan terrain is removed during the cycle run and subsequent forecasts. For the NoT run, GTS data (excluding observations from land-based stations over Taiwan), GPS RO refractivity profiles, and 18 TiMREX soundings at Dongsha, Penghu, and Lyudao stations (Fig. 1a) are assimilated for all three domains. At 1200 UTC 15 June, the subsynoptic distribution of TPW (Fig. 22a) in the NoT run is similar to the DA_ALL_DATA run (Fig. 3a). In the absence of island terrain, the early summer monsoon trough extends farther eastward toward western Taiwan (Figs. 22b and 22c) as compared to the DA_ALL_DATA run (Figs. 4a and 8a). The southwesterly flow prevails over the entire island of Taiwan (Fig. 22c). The cold pool is relatively weak over the southwestern coast of Taiwan (Figs. 22c and 22d) as compared to the DA_ALL_DATA run (Figs. 8a and 8b).

At 2100 UTC 15 June (0500 LT 16 June), the cold pool spreads eastward due to the presence of prevailing

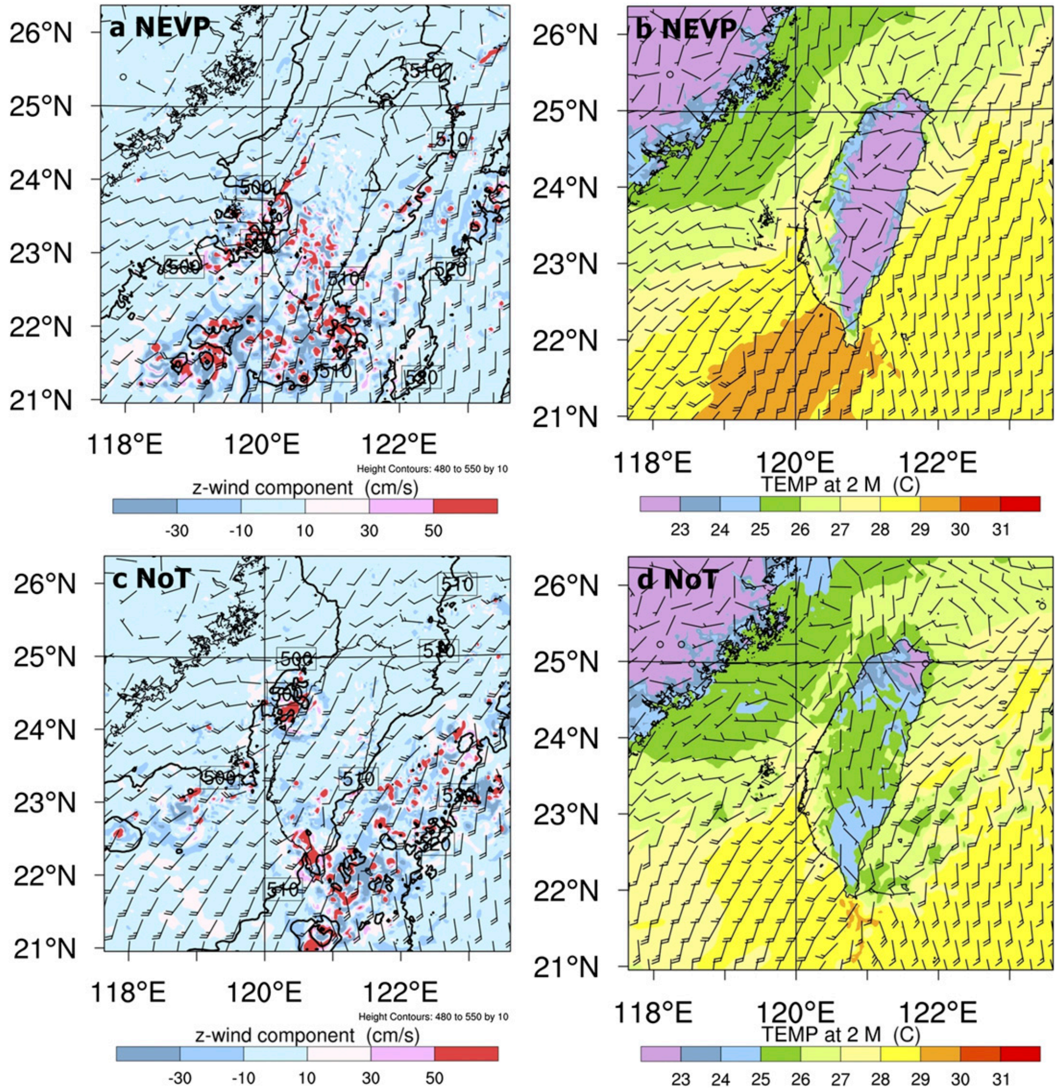

FIG. 18. Model forecasts for domain 3 valid at 2100 UTC 15 Jun. (a) The 950-hPa geopotential height (gpm) (contoured) and winds ($m\,s^{-1}$) (a full barb represents $5\,m\,s^{-1}$), and 700-hPa vertical velocity ($cm\,s^{-1}$) for the NEVP run. (b) The 2-m temperature (°C) and 10-m winds ($m\,s^{-1}$) (a full barb represents $5\,m\,s^{-1}$) for the NEVP run. (c),(d) As in (a),(b), but for the NoT run.

southwesterly monsoon flow (Fig. 17c). In low levels, the air temperature over the ocean off the southwestern coast is relatively warm. Thus, no rainfall is predicted off the southwestern coast (Fig. 19c) as compared to the DA_ALL_DATA run (Fig. 12c). At the surface, nocturnal cooling occurs over land with relatively weak winds over the island (Fig. 18d). Over southwestern Taiwan, the incoming southwesterly flow encounters the weak south-southeasterly flow over land (Fig. 18d) resulting in the coastal rainfall maximum (Fig. 19c). Without orographic blocking, however, the amount of nocturnal coastal rainfall is much smaller in the NoT run (Fig. 19c) than in the DA_ALL_DATA run (Fig. 12c).

During the daytime, without the presence of the CMR, the cold pool continues to spread out to the eastern side of Taiwan due to the presence of the prevailing southwesterly monsoon flow (Fig. 17d). As a result, flow deceleration upstream of southwestern Taiwan is not significant (Figs. 21c and 21d). The heavy rainfall off the southwestern coast of Taiwan is underestimated in the 3-km domain of the NoT run (Fig. 19d) as compared to the DA_ALL_DATA run (Fig. 15c) and observations (Figs. 15a and 15b) due to lack of orographic blocking and absence of the cold pool (Fig. 17d). In northern Taiwan, without the island wake (Fig. 20b) the sea-breeze/upslope flow is not simulated in the 3-km domain (Fig. 21d).

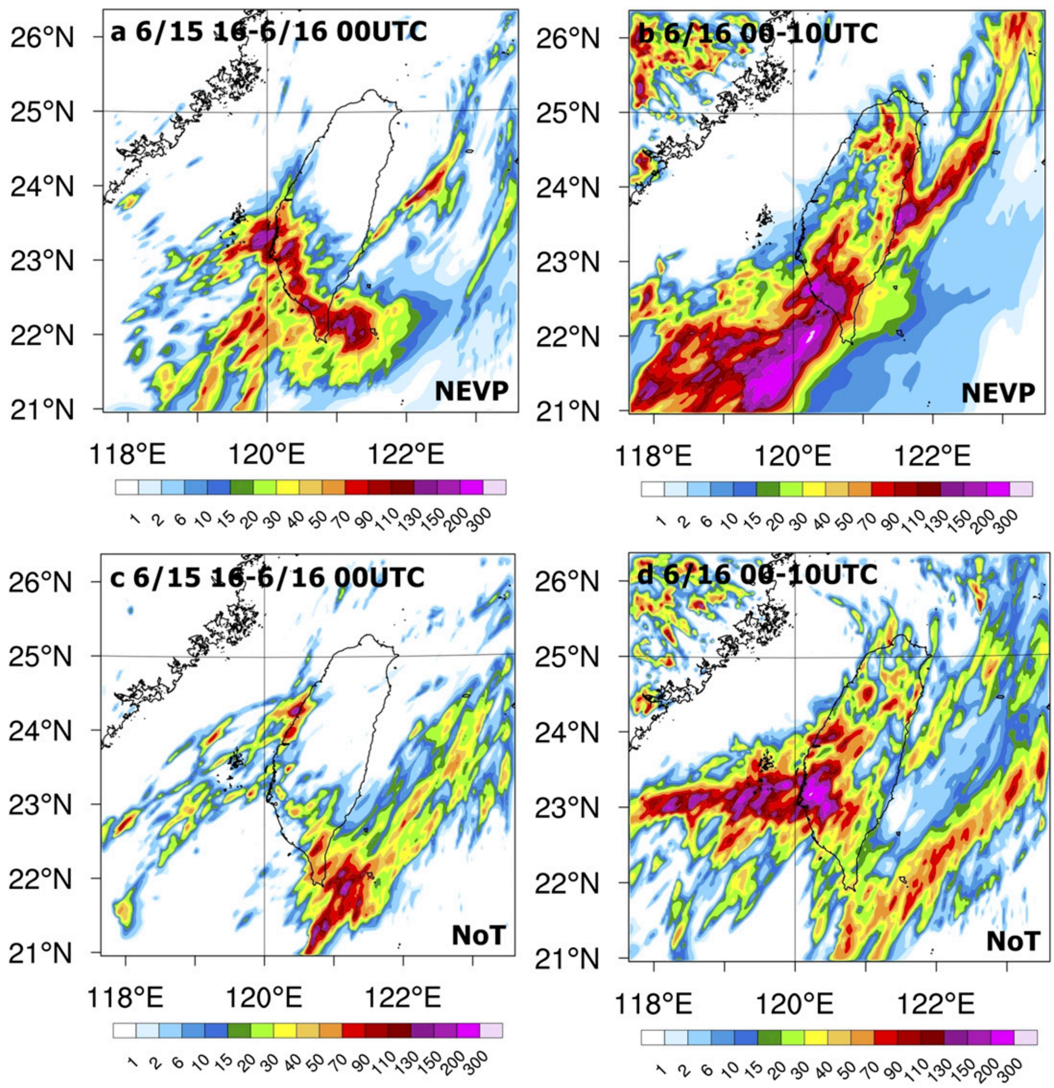

FIG. 19. Total rainfall accumulation (mm) during (a) 1600 UTC 15 Jun–0000 UTC 16 Jun and (b) 0000–1000 UTC 16 Jun from the NEVP run. (c),(d) As in (a),(b), but for the NoT run (domain 3).

As a result, isolated local heavy rainfall is not simulated over northern Taiwan in the NoT run (Fig. 19d).

During the daytime of 16 June, the early summer monsoon trough extends eastward toward western Taiwan in the NoT run (Figs. 20b and 21c) with relatively weak winds associated with the early summer monsoon trough off northwestern Taiwan (Fig. 20b). An east–west-oriented vertically integrated subsynoptic moisture flux convergence area computed from the domain 1 simulation extends from southwestern–western Taiwan westward to the southern part of the Taiwan Strait (Fig. 23), where the strong southwesterly flow encounters weak winds associated with the early summer monsoon trough (Figs. 20b and 23b). Furthermore, a weak upper-level trough is present off the southwestern coast (Tu et al. 2014). The simulated rainfall pattern from domain 3 (Fig. 19d) during the daytime resembles the simulated subsynoptic vertical integral of moisture convergence from domain 1 (Fig. 23a), indicating the subsynoptic control on rainfall production when the terrain is removed in the model. Furthermore, scattered rainfall showers are embedded within the southwesterly flow, especially on the windward side of Taiwan (Fig. 19d) where the incoming flow meets the weaker winds over land (Fig. 21d). From model sensitivity tests, it is apparent that including rain-evaporative cooling and orographic effects in the initial conditions and during the model time integration are important for the enhancement of orographic blocking and development of coastal rainfall.

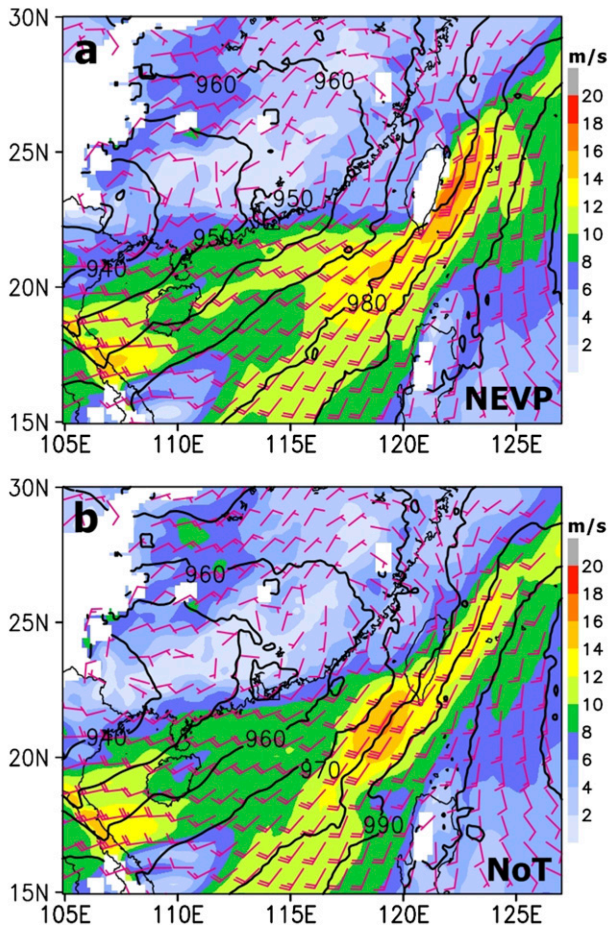

FIG. 20. Model forecasts of the averaged 900-hPa winds ($m\,s^{-1}$) (a full barb represents $5\,m\,s^{-1}$) and geopotential height in gpm (contoured) during 0000–1200 UTC 16 Jun for the domain 1. (a) NEVP run and (b) NoT run.

6. Summary

A cycling run that starts 36 h (0000 UTC 14 June–1200 UTC 15 June 2008) before the model forecast is used to assimilate TiMREX soundings, COSMIC GPS RO refractivity profiles, and GTS data to improve the model initial conditions at 1200 UTC 15 June (the DA_ALL_DATA run) provided by the NCEP GFS and subsequent forecasts of subsynoptic features, modifications of boundary layer over southwestern Taiwan by antecedent rains, orographic effects, and rainfall distributions for a heavy coastal rainfall case (15–16 June) during TiMREX. For the outer model domain (domain 1), we are able to prevent model drift of the large-scale flow during the cycling run by bringing in large-scale observational data (excluding TiMREX and GTS land-based observations over the Taiwan area) to generate better initial conditions (the DA_ALL_DATA run) as compared to the GFS data. For the DA_ALL_DATA run, both the southwesterly flow [or low-level jet (LLJ)] over the northern South China Sea and moisture tongue associated with LLJ are better depicted at the model initial time (1200 UTC 15 June) than the CTRL run initialized by the GFS analysis.

In addition to improvements in the depiction of the moisture tongue and LLJ over the northern South China Sea, the assimilation of all the available data also includes the effects of rain-evaporative cooling from antecedent rains during 14–15 June and orographic effects in the initial conditions of the nested domains. In the DA_ALL_DATA run, the initial and predicted air temperature below the 850-hPa level over southwestern Taiwan is relatively cold with significant orographic blocking upstream of the southwestern Taiwan coast, which is in agreement with observations. Above the cold pool, the decelerating southwesterly monsoon flow is deflected with a relatively large southerly wind component parallel to the terrain contours on the windward side of the north–south-oriented Central Mountain Range (CMR). During the daytime, an offshore wind component is predicted in low levels due to continued rain-evaporative cooling and extensive cloud cover over southwestern Taiwan. With significant flow deceleration and lifting of the incoming flow by the cold pool, heavy rainfall is predicted off the southwestern coast and coastal area and diminishes inland in the DA_ALL_DATA run.

In the CTRL run, without the effects of rain-evaporative cooling by antecedent rains and orographic blocking in the model initial conditions, the air in the boundary layer over southwestern Taiwan at the model initial time is relatively warm. Furthermore, the early summer monsoon trough over the southeastern China coast extends farther eastward over the Taiwan Strait and the incoming LLJ is stronger with a larger westerly component over southwestern Taiwan as compared to the DA_ALL_DATA run. A cold pool is predicted in the low levels during model integration due to significant orographic precipitation on the windward side as well as off the southwestern Taiwan coast. Because of a southeastward extension of the early summer monsoon trough toward the central Taiwan Strait, the overall rainfall pattern shifts southeastward during the daytime with higher rainfall amounts over the moisture tongue. Nevertheless, because of the presence of the cold pool over the southwestern coast and adjacent ocean, the predicted rainfall amount diminishes inland with higher rainfall along the coast than on the windward side of CMR. In addition to rainfall in the coastal areas, significant precipitation is predicted over southern tip of Taiwan.

The improved rainfall forecast over southwestern Taiwan and the adjacent coastal areas in the DA_ALL_DATA run is related to better prediction of the following features: warm, moist LLJ coming from the northern

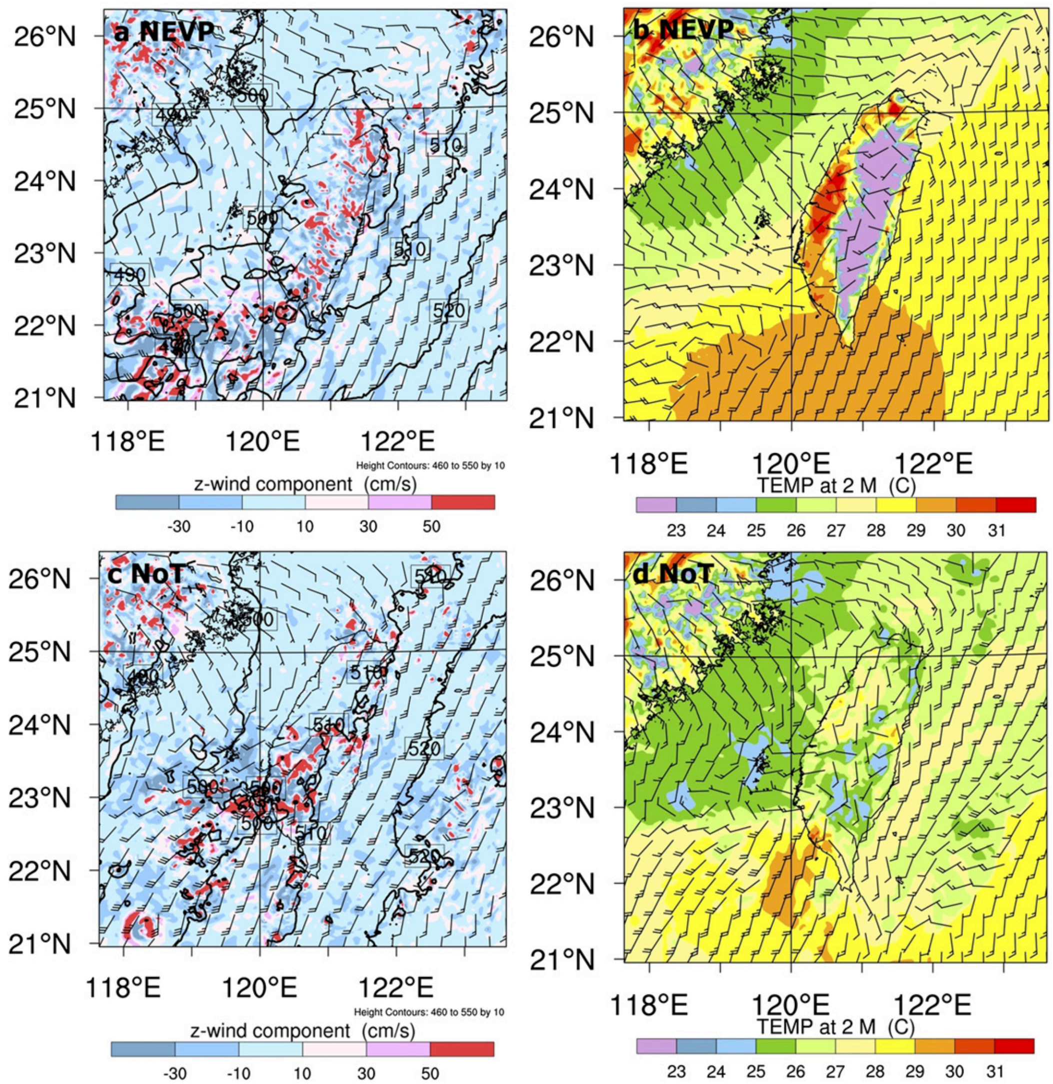

FIG. 21. As in Fig. 18, but for 0600 UTC 16 Jun.

South China Sea toward the southwestern Taiwan coast; significant blocking of the LLJ off the southwestern coast; cold pool due to rain-evaporative cooling resulting from antecedent rains with an offshore wind component at the surface in the model initial conditions and the subsequent forecast; and deflected southerly flow above the cold pool without significant orographic lifting on the windward slopes of the CMR.

We conducted model sensitivity tests to diagnose the effects of rain-evaporative cooling (NEVP run) and terrain (NoT run) on the intensity and depth of the cold pool and degree of orographic blocking on the southwesterly flow over southwestern Taiwan. It is apparent that rain-evaporative cooling not only produces a cold pool in the high-resolution (3 km) nested domain, but also alters the mesoscale flow. Without rain-evaporative cooling during model integration, the early summer monsoon trough over southeastern China extends eastward with a weaker southwesterly monsoon flow over the Taiwan area as compared to the DA_ALL_DATA run. Without rain-evaporative cooling during model integration (NEVP run), the cold pool in the 3-km nested domain (domain 3) gradually disappears with much weaker orographic blocking on the southwesterly flow off the southwestern Taiwan coast. As a result, the predicted maximum rainfall at night occurs along the southwestern coast where the incoming southwesterly flow encounters relatively weak south-southeasterly winds over the coastal area over southwestern Taiwan.

During the daytime, without the presence of the cold pool, flow deceleration of the LLJ off the southwestern coast is less significant when compared to the

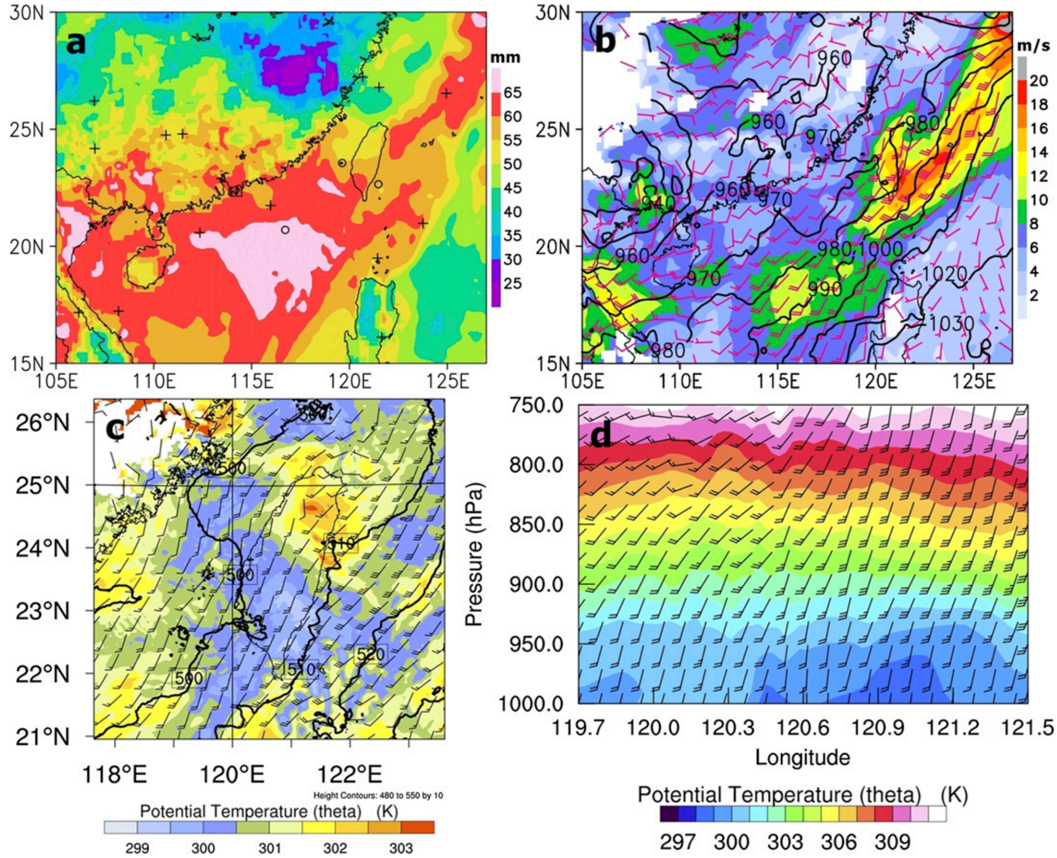

FIG. 22. Model initial conditions of the NoT run over domain 1 at 1200 UTC 15 Jun 2008 after the cycling run. (a) TPW (mm). The locations of soundings and GPS RO observations assimilated into the cycling run are indicated by circles and plus signs, respectively. (b) The 900-hPa geopotential height (gpm), wind speed (m s^{-1}) (shaded), and winds (m s^{-1}) (a full barb represents 5 m s^{-1}) from domain 1. (c) The 950-hPa potential temperature (K) (shaded), geopotential height (gpm) (contoured), and winds (m s^{-1}) (a full barb represents 5 m s^{-1}) from domain 3. (d) Vertical cross sections of potential temperature (K) (shaded) and winds (m s^{-1}) (a full barb represents 5 m s^{-1}) along line AB in Fig. 1a from domain 3.

DA_ALL_DATA run. Above the 900-hPa level, the incoming large-scale southwesterly flow has a westerly wind component impinging on CMR. In addition, the upslope flow prevails at low levels over southwestern Taiwan. As a result, in addition to widespread rainfall over the northern South China Sea and windward coastal areas, significant orographic precipitation is predicted on the southwestern slopes of CMR.

The impact of orographic effects on focusing coastal rainfall is also addressed with the island terrain component removed during the cycling run and subsequent forecast (NoT run). For the NoT run, the GPS RO refractivity profiles, GTS data (excluding land-based observations over Taiwan), and 18 TiMREX data from three outer island stations (Dongsha, Penghu, and Lyudao) are assimilated during the cycling run. The large-scale initial conditions at 1200 UTC 15 June are similar to the DA_ALL_DATA run. Over the high-resolution (3 km) nested domain, a cold pool is simulated at low levels over the Taiwan area due to antecedent rains. At night, an offshore wind component is predicted at the surface over southwestern Taiwan with weak winds over the island. The nocturnal coastal rainfall in the NoT run, which is the result of the convergence between the southwesterly flow and the offshore flow, is weaker than the DA_ALL_DATA run due to the absence of island terrain in the model.

Without the presence of CMR in the NoT run, the cold pool spreads out to the eastern side of Taiwan during the daytime due to the presence of the prevailing southwesterly monsoon flow. The flow deceleration upstream of southwestern Taiwan is less significant as compared to the DA_ALL_DATA run. The heavy rainfall off the southwest coast of Taiwan is underestimated in the NoT run as compared to the DA_ALL_DATA run and observations due to the lack of blocking

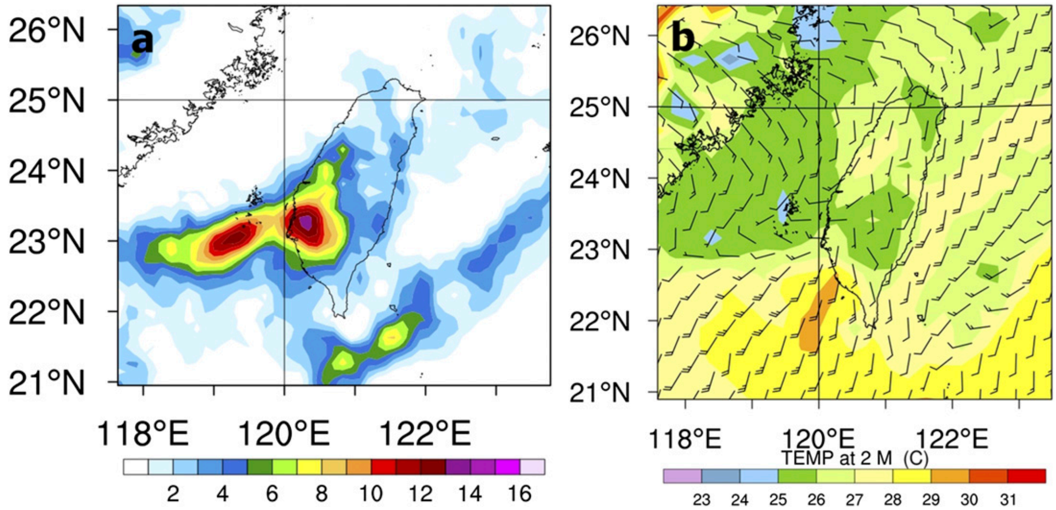

FIG. 23. (a) Domain 1 averaged vertically integrated moisture flux convergence (mm h^{-1}) during 0000–1000 UTC 16 Jun, and (b) 2-m temperature (°C) and 10-m winds (m s^{-1}) (a full barb represents 5 m s^{-1}) at 0600 UTC 16 Jun for the NoT run.

effect of terrain and absence of a cold pool without an offshore wind component in the model simulation. Instead, an east–west-oriented rainy area extends from southwestern Taiwan westward to the southern Taiwan Strait where the large-scale vertically integrated moisture convergence occurs. Furthermore, convective showers are predicted within the southwesterly monsoon flow over the island, especially on the windward side as the incoming southwesterly flow encounters weaker winds inland.

In the future, additional coastal rainfall events over southwestern Taiwan during the early summer rainy season will be studied and compared with this case. Furthermore, for this case, the heavy coastal rainfall is under the influence of the strong and moist southwesterly monsoon flow [or the low-level jet (LLJ)] over the northern South China Sea (Fig. 13; Xu et al. 2012) in the prefrontal environment with maximum wind speed occurring within the boundary layer (around the 900-hPa level). This type of LLJ event is apparently different from the LLJs associated with the subsynoptic frontal systems during the early summer rainy season found in the literature, which have maximum wind speed within the 700–850-hPa level (e.g., Chen and Yu 1988; Chen et al. 1994; and others). Work in this area is currently under way.

Acknowledgments. The authors thank all the participants of TiMREX for their dedication and efforts. This work is funded jointly by the National Science Foundation under Grant AGS-1142558, NOAA under Cooperative Agreement NA11NOS0120039, and NCAR under the Advanced Study Program (ASP). The work is also partially funded by the Taiwan National Science Council (NSC) under Grant NSC-100-2119-M-008-041-MY5 and Ministry of Science and Technology (MOST) under Grant MOST 104-2923-M-008-003-MY5. We thank Dr. C.-T. Fong (CWB) and Mr. C. H. Chiang (CWB) for providing the TiMREX and satellite data for data assimilation, Dr. J.-S. Hong (CWB) for providing the land-use data for the Noah land surface model, and May Izumi for editing the text.

REFERENCES

Anthes, R. A., 2011: Exploring Earth's atmosphere with radio occultation: Contributions to weather, climate and space weather. *Atmos. Meas. Tech.*, **4**, 1077–1103, doi:10.5194/amt-4-1077-2011.

Barker, D. M., W. Huang, Y.-R. Guo, A. J. Bourgeois, and Q. N. Xiao, 2004: A three-dimensional variational data assimilation system for MM5: Implementation and initial results. *Mon. Wea. Rev.*, **132**, 897–914, doi:10.1175/1520-0493(2004)132<0897:ATVDAS>2.0.CO;2.

Chen, C.-S., Y.-L. Chen, C.-L. Liu, P.-L. Lin, and W.-C. Chen, 2007: Statistics of heavy rainfall occurrences in Taiwan. *Wea. Forecasting*, **22**, 981–1002, doi:10.1175/WAF1033.1.

Chen, F., and J. Dudhia, 2001: Coupling an advanced land surface–hydrology model with the Penn State–NCAR MM5 modeling system. Part I: Model implementation and sensitivity. *Mon. Wea. Rev.*, **129**, 569–585, doi:10.1175/1520-0493(2001)129<0569:CAALSH>2.0.CO;2.

Chen, S.-Y., C.-Y. Huang, Y.-H. Kuo, Y.-R. Guo, and S. Sokolovskiy, 2009: Assimilation of GPS refractivity from FORMOSAT-3/COSMIC using a nonlocal operator with WRF 3DVAR and its impact on the prediction of a typhoon event. *Terr. Atmos. Oceanic Sci.*, **20**, 133–154, doi:10.3319/TAO.2007.11.29.01(F3C).

——, ——, ——, and S. Sokolovskiy, 2011: Observational error estimation of FORMOSAT-3/COSMIC GPS radio occultation data. *Mon. Wea. Rev.*, **139**, 853–865, doi:10.1175/2010MWR3260.1.

——, T.-K. Wee, Y.-H. Kuo, and D. H. Bromwich, 2014: An impact assessment of GPS radio occultation data on prediction of a rapidly developing cyclone over the Southern Ocean. *Mon. Wea. Rev.*, **142**, 4187–4206, doi:10.1175/MWR-D-14-00024.1.

Chen, G. T.-J., and C.-C. Yu, 1988: Study of low-level jet and extremely heavy rainfall over northern Taiwan in the mei-yu season. *Mon. Wea. Rev.*, **116**, 884–891, doi:10.1175/1520-0493(1988)116<0884:SOLLJA>2.0.CO;2.

Chen, Y.-L., and N. B.-F. Hui, 1990: Analysis of a shallow front during the Taiwan Area Mesoscale Experiment. *Mon. Wea. Rev.*, **118**, 2649–2667, doi:10.1175/1520-0493(1990)118<2649:AOASFD>2.0.CO;2.

——, and J. Li, 1995a: Characteristics of surface airflow and pressure patterns over the island of Taiwan during TAMEX. *Mon. Wea. Rev.*, **123**, 695–716, doi:10.1175/1520-0493(1995)123<0695:COSAAP>2.0.CO;2.

——, and ——, 1995b: Large-scale conditions favorable for the development of heavy rainfall during TAMEX IOP 3. *Mon. Wea. Rev.*, **123**, 2978–3002, doi:10.1175/1520-0493(1995)123<2978:LSCFFT>2.0.CO;2.

——, Y.-X. Zhang, and N. B.-F. Hui, 1989: Analysis of a surface front during the early summer rainy season over Taiwan. *Mon. Wea. Rev.*, **117**, 909–931, doi:10.1175/1520-0493(1989)117<0909:AOASFD>2.0.CO;2.

——, X. A. Chen, and Y.-X. Zhang, 1994: A diagnostic study of the low-level jet during TAMEX IOP 5. *Mon. Wea. Rev.*, **122**, 2257–2284, doi:10.1175/1520-0493(1994)122<2257:ADSOTL>2.0.CO;2.

Chien, F.-C., and B. J.-D. Jou, 2004: MM5 ensemble mean precipitation forecasts in the Taiwan area for three early summer convective (mei-yu) seasons. *Wea. Forecasting*, **19**, 735–750, doi:10.1175/1520-0434(2004)019<0735:MEMPFI>2.0.CO;2.

Chou, M.-D., and M. J. Suarez, 1994: An efficient thermal infrared radiation parameterization for use in general circulation models. NASA Tech. Memo. 104606, Vol. 3, 85 pp.

Ciesielski, P. E., and Coauthors, 2010: Quality-controlled upper-air sounding dataset for TiMREX/SoWMEX: Development and corrections. *J. Atmos. Oceanic Technol.*, **27**, 1802–1821, doi:10.1175/2010JTECHA1481.1.

Cucurull, L., J. C. Derber, and R. J. Purser, 2013: A bending angle forward operator for global positioning system radio occultation measurements. *J. Geophys. Res. Atmos.*, **118**, 14–28, doi:10.1029/2012JD017782.

Daley, R., 1991: *Atmospheric Data Analysis.* Cambridge University Press, 457 pp.

Dyer, A. J., and B. B. Hicks, 1970: Flux-gradient relationships in the constant flux layer. *Quart. J. Roy. Meteor. Soc.*, **96**, 715–721, doi:10.1002/qj.49709641012.

Gemmill, W., B. Katz, and X. Li, 2007: Daily real-time global sea surface temperature-high resolution analysis at NOAA/NCEP. NOAA/NWS/NCEP/MMAB Office Note 260, 39 pp.

Hajj, G. A., and Coauthors, 2004: CHAMP and SAC-C atmospheric occultation results and intercomparisons. *J. Geophys. Res.*, **109**, D06109, doi:10.1029/2003JD003909.

Healy, S. B., J. R. Eyre, M. Hamrud, and J.-N. Thépaut, 2007: Assimilating GPS radio occultation measurements with two-dimensional bending angle observation operators. *Quart. J. Roy. Meteor. Soc.*, **133**, 1213–1227, doi:10.1002/qj.63.

Hong, S.-Y., Y. Noh, and J. Dudhia, 2006: A new vertical diffusion package with an explicit treatment of entrainment processes. *Mon. Wea. Rev.*, **134**, 2318–2341, doi:10.1175/MWR3199.1.

Hsiao, L.-F., D.-S. Chen, Y.-H. Kuo, Y.-R. Guo, T.-C. Yeh, J.-S. Hong, C.-T. Fong, and C.-S. Lee, 2012: Application of WRF 3DVAR to operational typhoon prediction in Taiwan: Impact of outer loop and partial cycling approaches. *Wea. Forecasting*, **27**, 1249–1263, doi:10.1175/WAF-D-11-00131.1.

Huang, C.-Y., Y.-H. Kuo, S.-H. Chen, and F. Vandenberghe, 2005: Improvements in typhoon forecasts with assimilated GPS occultation refractivity. *Wea. Forecasting*, **20**, 931–953, doi:10.1175/WAF874.1.

Ide, K., P. Courtier, M. Ghil, and A. C. Lorenc, 1997: Unified notation for data assimilation: Operational, sequential and variational. *J. Meteor. Soc. Japan*, **75**, 181–189.

Joyce, R. J., J. E. Janowiak, P. A. Arkin, and P. Xie, 2004: CMORPH: A method that produces global precipitation estimates from passive microwave and infrared data at high spatial and temporal resolution. *J. Hydrometeor.*, **5**, 487–503, doi:10.1175/1525-7541(2004)005<0487:CAMTPG>2.0.CO;2.

Kain, J. S., 2004: The Kain–Fritsch convective parameterization: An update. *J. Appl. Meteor.*, **43**, 170–181, doi:10.1175/1520-0450(2004)043<0170:TKCPAU>2.0.CO;2.

Kerns, B. W. J., Y.-L. Chen, and M.-Y. Chang, 2010: The diurnal cycle of winds, rain, and clouds over Taiwan during the mei-yu, summer, and autumn rainfall regimes. *Mon. Wea. Rev.*, **138**, 497–516, doi:10.1175/2009MWR3031.1.

Kuo, Y.-H., S. Sokolovskiy, R. A. Anthes, and F. Vandenberghe, 2000: Assimilation of GPS radio occultation data for numerical weather prediction. *Terr. Atmos. Oceanic Sci.*, **11**, 157–186.

——, T.-K. Wee, S. Sokolovskiy, C. Rocken, W. Schreiner, D. Hunt, and R. A. Anthes, 2004: Inversion and error estimation of GPS radio occultation data. *J. Meteor. Soc. Japan*, **82**, 507–531, doi:10.2151/jmsj.2004.507.

——, W. S. Schreiner, J. Wang, D. L. Rossiter, and Y. Zhang, 2005: Comparison of GPS radio occultation soundings with radiosondes. *Geophys. Res. Lett.*, **32**, L05817, doi:10.1029/2004GL021443.

Laprise, R., 1992: The Euler equations of motion with hydrostatic pressure as an independent variable. *Mon. Wea. Rev.*, **120**, 197–207, doi:10.1175/1520-0493(1992)120<0197:TEEOMW>2.0.CO;2.

Lin, P.-L., Y.-L. Chen, C.-S. Chen, C.-L. Liu, and C.-Y. Chen, 2011: Numerical experiments investigating the orographic effects on a heavy rainfall event over the northwestern coast of Taiwan during TAMEX IOP 13. *Meteor. Atmos. Phys.*, **114**, 35–50, doi:10.1007/s00703-011-0155-7.

Lorenc, A. C., 1986: Analysis methods for numerical weather prediction. *Quart. J. Roy. Meteor. Soc.*, **112**, 1177–1194, doi:10.1002/qj.49711247414.

Mlawer, E. J., S. J. Taubman, P. D. Brown, M. J. Iacono, and S. A. Clough, 1997: Radiative transfer for inhomogeneous atmospheres: RRTM, a validated correlated-k model for the longwave. *J. Geophys. Res.*, **102**, 16 663–16 682, doi:10.1029/97JD00237.

Moncrieff, M. W., D. E. Waliser, M. J. Miller, M. A. Shapiro, G. R. Asrar, and J. Caughey, 2012: Multiscale convective organization and the YOTC virtual global field campaign. *Bull. Amer. Meteor. Soc.*, **93**, 1171–1187, doi:10.1175/BAMS-D-11-00233.1.

Parrish, D. F., and J. C. Derber, 1992: The National Meteorological Center's spectral statistical-interpolation analysis system. *Mon. Wea. Rev.*, **120**, 1747–1763, doi:10.1175/1520-0493(1992)120<1747:TNMCSS>2.0.CO;2.

Paulson, C. A., 1970: The mathematical representation of wind speed and temperature profiles in the unstable atmospheric surface layer. *J. Appl. Meteor.*, **9**, 857–861, doi:10.1175/1520-0450(1970)009<0857:TMROWS>2.0.CO;2.

Rocken, C., and Coauthors, 1997: Analysis and validation of GPS/MET data in the neutral atmosphere. *J. Geophys. Res.*, **102**, 29 849–29 866, doi:10.1029/97JD02400.

Rogers, E., D. Parrish, Y. Lin, and G. DiMego, 1996: The NCEP Eta data assimilation system: Tests with regional 3-D variational analysis and cycling. Preprints, *11th Conf. on Numerical Weather Prediction*, Norfolk, VA, Amer. Meteor. Soc., 105–106.

Ruppert, J. H., Jr., R. H. Johnson, and A. K. Rowe, 2013: Diurnal circulations and rainfall in Taiwan during SoWMEX/TiMREX (2008). *Mon. Wea. Rev.*, **141**, 3851–3872, doi:10.1175/MWR-D-12-00301.1.

Skamarock, W. C., and Coauthors, 2008: A description of the Advanced Research WRF version 3. NCAR Tech. Note NCAR/TN-475+STR, 113 pp., 10.5065/D68S4MVH.

Smith, E. K., and S. Weintraub, 1953: The constants in the equation for the atmospheric refractive index at radio frequencies. *Proc. IRE*, **41**, 1035–1037, doi:10.1109/JRPROC.1953.274297.

Smith, R. B., 1989: Mountain-induced stagnation points in hydrostatic flow. *Tellus*, **41A**, 270–274, doi:10.1111/j.1600-0870.1989.tb00381.x.

Smolarkiewicz, P. K., R. M. Rasmussen, and T. L. Clark, 1988: On the dynamics of Hawaiian cloud bands: Island forcing. *J. Atmos. Sci.*, **45**, 1872–1905, doi:10.1175/1520-0469(1988)045<1872:OTDOHC>2.0.CO;2.

Sun, W.-Y., J.-D. Chern, C.-C. Wu, and W.-R. Hsu, 1991: Numerical simulation of mesoscale circulation in Taiwan and surrounding area. *Mon. Wea. Rev.*, **119**, 2558–2573, doi:10.1175/1520-0493(1991)119<2558:NSOMCI>2.0.CO;2.

Tao, W.-K., and J. Simpson, 1993: The Goddard cumulus ensemble model. Part I: Model description. *Terr. Atmos. Oceanic Sci.*, **4**, 35–72.

——, and Coauthors, 2013: Precipitation intensity and variation during MC3E: A numerical modeling study. *J. Geophys. Res. Atmos.*, **118**, 7199–7218, doi:10.1002/jgrd.50410.

Trier, S. B., D. B. Parsons, and T. J. Matejka, 1990: Observations of a subtropical cold front in a region of complex terrain. *Mon. Wea. Rev.*, **118**, 2449–2470, doi:10.1175/1520-0493(1990)118<2449:OOASCF>2.0.CO;2.

Tu, C.-C., Y.-L. Chen, C.-S. Chen, P.-L. Lin, and P.-H. Lin, 2014: A comparison of two heavy rainfall events during the Terrain-influenced Monsoon Rainfall Experiment (TiMREX) 2008. *Mon. Wea. Rev.*, **142**, 2436–2463, doi:10.1175/MWR-D-13-00293.1.

Wang, C.-C., J. C.-S. Hsu, G. T.-J. Chen, and D.-I. Lee, 2014a: A study of two propagating heavy-rainfall episodes near Taiwan during SoWMEX/TiMREX IOP-8 in June 2008. Part I: Synoptic evolution, episode propagation, and model control simulation. *Mon. Wea. Rev.*, **142**, 2619–2643, doi:10.1175/MWR-D-13-00331.1.

——, ——, ——, and ——, 2014b: A study of two propagating heavy-rainfall episodes near Taiwan during SoWMEX/TiMREX IOP-8 in June 2008. Part II: Sensitivity tests on the roles of synoptic conditions and topographic effects. *Mon. Wea. Rev.*, **142**, 2644–2664, doi:10.1175/MWR-D-13-00330.1.

Webb, E. K., 1970: Profile relationships: The log-linear range, and extension to strong stability. *Quart. J. Roy. Meteor. Soc.*, **96**, 67–90, doi:10.1002/qj.49709640708.

Wickert, J., T. Schmidt, G. Beyerle, R. König, C. Reigber, and N. Jakowski, 2004: The radio occultation experiment aboard CHAMP: Operational data analysis and validation of vertical atmospheric profiles. *J. Meteor. Soc. Japan*, **82**, 381–395, doi:10.2151/jmsj.2004.381.

Xu, W., E. J. Zipser, Y.-L. Chen, C. Liu, Y.-C. Liou, W.-C. Lee, and B. J.-D. Jou, 2012: An orography-associated extreme rainfall event during TiMREX: Initiation, storm evolution, and maintenance. *Mon. Wea. Rev.*, **140**, 2555–2574, doi:10.1175/MWR-D-11-00208.1.

Yang, M.-J., and R. A. Houze Jr., 1995: Sensitivity of squall-line rear inflow to ice microphysics and environmental humidity. *Mon. Wea. Rev.*, **123**, 3175–3193, doi:10.1175/1520-0493(1995)123<3175:SOSLRI>2.0.CO;2.

Yang, S.-C., S.-H. Chen, S.-Y. Chen, C.-Y. Huang, and C.-S. Chen, 2014: Evaluating the impact of the COSMIC RO bending angle data on predicting the heavy precipitation episode on 16 June 2008 during SoWMEX-IOP8. *Mon. Wea. Rev.*, **142**, 4139–4163, doi:10.1175/MWR-D-13-00275.1.

Yeh, H.-C., and Y.-L. Chen, 1998: Characteristics of the rainfall distributions over Taiwan during the Taiwan Area Mesoscale Experiment (TAMEX). *J. Appl. Meteor.*, **37**, 1457–1469, doi:10.1175/1520-0450(1998)037<1457:CORDOT>2.0.CO;2.

——, and ——, 2003: Numerical simulations of the barrier jet over northwestern Taiwan during the mei-yu season. *Mon. Wea. Rev.*, **131**, 1396–1407, doi:10.1175/1520-0493(2003)131<1396:NSOTBJ>2.0.CO;2.

Zhu, T., and D.-L. Zhang, 2006: Numerical simulation of Hurricane Bonnie (1998). Part II: Sensitivity to varying cloud microphysical processes. *J. Atmos. Sci.*, **63**, 109–126, doi:10.1175/JAS3599.1.